12-1-2013

Nonlinear Adaptive Diffusion Models for Image Denoising

Ajay Kumar Mandava
University of Nevada, Las Vegas

NONLINEAR ADAPTIVE DIFFUSION MODELS FOR IMAGE DENOISING

by

Ajay Kumar Mandava

Bachelor of Technology in Electronics and Communication Engineering

Jawaharlal Nehru Technological University, India

May 2006

Master of Science in Electrical Engineering

University of Nevada Las Vegas, USA

December 2009

A dissertation submitted in partial fulfillment

of the requirements for the

Doctor of Philosophy - Electrical Engineering

Department of Electrical and Computer Engineering

Howard R. Hughes College of Engineering

The Graduate College

University of Nevada, Las Vegas

December 2013

UNLV
UNIVERSITY OF NEVADA LAS VEGAS

THE GRADUATE COLLEGE

We recommend the dissertation prepared under our supervision by

Ajay Kumar Mandava

entitled

Nonlinear Adaptive Diffusion Models for Image Denoising

is approved in partial fulfillment of the requirements for the degree of

Doctor of Philosophy in Engineering - Electrical Engineering

Department of Electrical and Computer Engineering

Emma Regentova, Ph.D., Committee Chair

Henry Selvaraj, Ph.D., Committee Member

Shahram Latifi, Ph.D., Committee Member

Venkatesan Muthukumar, Ph.D., Committee Member

Ajoy Datta, Ph.D., Graduate College Representative

Kathryn Hausbeck Korgan, Ph.D., Interim Dean of the Graduate College

December 2013

ABSTRACT

Nonlinear Adaptive Diffusion Models for Image Denoising

by

Ajay Kumar Mandava

Dr. Emma E. Regentova, Examination Committee Chair
Associate Professor of Electrical and Computer Engineering
University of Nevada, Las Vegas

Most of digital image applications demand on high image quality. Unfortunately, images often are degraded by noise during the formation, transmission, and recording processes. Hence, image denoising is an essential processing step preceding visual and automated analyses. Image denoising methods can reduce image contrast, create block or ring artifacts in the process of denoising. In this dissertation, we develop high performance non-linear diffusion based image denoising methods, capable to preserve edges and maintain high visual quality. This is attained by different approaches: First, a nonlinear diffusion is presented with robust M-estimators as diffusivity functions. Secondly, the knowledge of textons derived from Local Binary Patterns (LBP) which unify divergent statistical and structural models of the region analysis is utilized to adjust the time step of diffusion process. Next, the role of nonlinear diffusion which is adaptive to the local context in the wavelet domain is investigated, and the stationary wavelet context based diffusion (SWCD) is developed for performing the iterative shrinkage. Finally, we develop a locally- and feature-adaptive diffusion (LFAD) method, where each image patch/region is diffused individually, and the diffusivity function is modified to incorporate the Inverse Difference Moment as a local estimate of the gradient.

Experiments have been conducted to evaluate the performance of each of the developed method and compare it to the reference group and to the state-of-the-art methods.

ACKNOWLEDGMENTS

It is with immense gratitude that I acknowledge the support and help of Dr. Emma E. Regentova. This dissertation would not have been possible without her dedication and guidance through all my doctorate years. I would like to thank her for all the opportunities she put in front of me, for her friendship and help in other aspects of my life. It has been a great experience and fun working with her in both the research and the classes.

Thanks to the Dr. Markus Berli and Desert Research Institute for providing the funds for my first year of my doctorate. I am grateful to the Department of Electrical and Computer Engineering and its chair for the financial assistantship and other support they provided during my studies. Also, I would like to thank Dr. Karen Egiazarian, Dr. George Bebis, Dr. Shahram Latifi, Dr. Muthukumar Venkatesan, Dr. Ajoy K. Datta, and Dr. Henry Selvaraj for their direct and indirect contribution throughout this dissertation.

Finally, I would like to give special thanks to my family and friends for their continuing love and affection throughout my life and career.

This work was partially supported by National Science Foundation under Grants No. DEB- 0817073 and 0816726, NASA EPSCoR under Cooperative Agreement No. NNX10AR89A, UNLV Graduate Assistantship, UNLV Access Grant-Grad NN, Spring 2011- Spring 2013, UNLV Summer Session Scholarship, 2010 & 2011 and UNLV Graduate and Professional Student Association (GPSA) grant 2012.

TABLE OF CONTENTS

LIST OF TABLES

LIST OF FIGURES

CHAPTER # 1

INTRODUCTION

This chapter defines the problem of image denoising and describes the importance of image denoising. Also discussed are various measures to evaluate image denoising results and given a brief overview of some of the advanced methods and research directions. Finally, this chapter summarizes contributions made by the dissertation.

1.1 Problem definition: What is image denoising?

Image denoising is the problem of finding a “clean” image, given a noisy one. In most cases, it is assumed that the noisy image is the sum of an underlying clean image and a noise component, see Fig 1.1. Hence image denoising is a decomposition problem. Since an infinite number of such decompositions exist, one is interested in finding a reliable clean image, given a noisy one. The notion of “reliable” is not clearly defined, but the idea is that the denoised image should look like an image, whereas the noise component should look noisy. The notion of “reliable” therefore involves prior knowledge: One knows something about images and about the noise. Without any prior knowledge, image denoising would be impossible.

Fig 1.1. A noisy image is the sum of the underlying clean image and the noise.

1.2 Sources and types of noise

During any physical measurement, it is likely that the signal acquisition process is corrupted by some amount of noise. The sources and types of noise depend on the physical measurement. Noise often comes from a source that is different from the one to be measured (e.g. read-out noise in digital cameras), but sometimes is due to the measurement process itself (e.g. photon shot noise). Sometimes, noise might be due to the mathematical manipulation of a signal, as is the case in image deconvolution or image compression. Often, a measurement is corrupted by several sources of noise and it is usually difficult to fully characterize all of them. In all cases, noise is the undesirable part of the signal. Ideally, one seeks to reduce noise by manipulating the signal acquisition process, but when such a modification is impossible, denoising algorithms are required. The characteristics of the noise depend on the signal acquisition process. Images can be acquired in a number of ways, including, but not limited to: Digital and analog cameras of various kinds (e.g. for visible or infra-red light), magnetic resonance imaging (MRI), computed tomography (CT), positron-emission tomography (PET), ultrasonography, electron microscopy and radar imagery such as synthetic aperture radar (SAR). The following is a list of possible types of noise.

Additive white Gaussian noise: Probably the most frequently occurring noise is additive white Gaussian noise (AWGN). For each pixel, a random value drawn from a normal distribution is added to the clean pixel value. The distribution is the same for every pixel (i.e. the mean and variance are the same) and the noise samples are drawn independently of each other. The read-out noise of digital cameras is often approximately AWGN. An example of an image corrupted with AWG noise is shown in Fig 1.1.

Salt and Pepper Noise: Salt and pepper noise refers to a wide variety of processes that result in the same basic image degradation: only a few pixels are noisy, but they are very noisy. The effect is similar to sprinkling white and black dots—salt and pepper—on the image. One example where salt and pepper noise arises is in transmitting images over noisy digital links.

Speckle noise: Speckle noise is a granular noise that inherently exists in and degrades the quality of images. Speckle noise is a multiplicative noise, i.e. it is in direct proportion to the local grey level in any area. The signal and the noise are statistically independent of each other. When coherent light strikes a surface, it is reflected back. Due to the microscopic variations in the surface roughness within one pixel, the received signal is subjected to random variations in phase and amplitude. Some of these variations in phase add constructively, resulting in strong intensities, and others add deconstructively, resulting in low intensities. This variation is called speckle.

Poisson noise: Fundamentally, most image acquisition devices are photon counters. Let 'a' denote the number of photons counted at some location (a pixel) in an image. Then, the distribution is usually modeled as Poisson with parameter λ. This noise is also called Photon noise or Poisson counting noise.

$$P(a = k) = \frac{e^{-\lambda}\lambda^{k}}{k!}$$

Quantization and Uniform Noise: Quantization noise results when a continuous random variable is converted to a discrete one or when a discrete random variable is converted to one with fewer levels. In images, quantization noise often occurs in the acquisition process. The image may be continuous initially, but to be processed it must be converted

to a digital representation. When the number of quantization levels is small, the quantization noise becomes signal dependent. In an image of the noise, signal features can be discerned. Also, the noise is correlated on a pixel by pixel basis and not uniformly distributed.

Thermal noise: Thermal noise arises due to the thermal energy of a chip. Thermally generated electrons accumulate in the chip's wells and are indistinguishable from photoelectrons. Thermal noise occurs even in the absence of light and is therefore sometimes referred to as dark-current noise. This type of noise is strongly dependent on the temperate of the sensor, but also on exposure time as well as the ISO-setting of the camera. Each pixel can be approximately modeled as a Gaussian. Thermal noise is an example of noise which can be reduced by modifying the signal acquisition process: Cooling the camera's sensor reduces thermal noise.

Rician noise: Magnetic resonance images are usually corrupted by Rician noise. In MRI data, each pixel consists of a complex number. For viewing MRI data, the absolute value of each complex number is taken. If the real and imaginary parts of the complex number are Gaussian-distributed and independent (with the same variance), the absolute value is Rician-distributed. Similarly to the Poisson distribution, the Rician distribution can be well approximated with a Gaussian distribution, for higher mean values.

Summary: Sources and types of noise are numerous and diverse and occur in almost all imaging settings. When designing a denoising method, prior knowledge about the noise has to be adapted depending on the type of noise. The situation generally becomes more difficult when several types of noise affect the image.

1.3 Evaluating denoising outcome

After denoising an image, we would like to know: How good is the denoising result? In asking this, we are actually inquiring the following:

(i) How close is the denoising result to the underlying true (clean) image?

(ii) How good does the denoised image look? One could imagine extremes in both scenarios.

Finding a good answer to this question is important in image denoising, because denoising almost inevitably introduces new distortion. Hence it is important to know which of those are the most or least disturbing. In evaluating image quality there are two followed methods, the subjective and the objective criteria. The subjective evaluation is considered costly, expensive, and time consuming; since we have to select a number of observers, show then a number of images and ask them to score images quality depending on their own opinion. However, this solution is too inconvenient for many applications. Hence, one is interested in automatic image quality assessment and in particular in objective image quality metrics that correlate with subjective image quality. Image quality metrics can be divided into two categories: (i) Full-reference, and (ii) no-reference. Full-reference metrics assume that the true underlying image is available in order to compute a measure, whereas no-reference metrics perform a blind quality assessment: The true underlying image is not available.

Mean Squared Error: The common performance criterion which is a full-reference metric is the mean squared error (MSE):

$$MSE = E\left[\left(f - \hat{f}\right)^2\right]$$

Peak Signal to Noise Ratio: The most commonly used metric for image quality assessment is the peak signal to Noise ratio (PSNR), which is a full-reference metric and calculated between two images x and y as follows:

$$PSNR = 10\log_{10}\left(\frac{MAX^2}{MSE}\right)$$

where MAX is the maximum pixel value, e.g., 255 for 8 bit images. The PSNR is perhaps the simplest of all image quality metrics. Still, higher dB values tend to correlate with higher visual similarity between the two images x and y. However, higher dB values do not always indicate higher visual similarity, which is why extensive effort has been put into finding alternative metrics.

Other Metrics: Some image quality metrics attempt to exploit known characteristics of the human visual system. The Universal image quality index (UIQI) [1] and structural similarity index (SSIM) [2]are full reference methods. SSIM image quality metric separates the task of similarity measurement into three components: (i) luminance, (ii) contrast, and (iii) structure. Among other things, the SSIM takes into account that the human visual system is sensitive to relative changes in luminance, rather than to absolute changes in luminance. The SSIM is a measure that is smaller or equal to 1. The measure is equal to 1 only in case the two images being compared are identical. Variants of the SSIM include a multi-scale extension (MS-SSIM [3]) and the information content weighted SSIM (IW-SSIM [4]). Other full-reference image quality metrics include the information-content weighted PSNR (IW-PSNR [4]), the information fidelity criterion (IFC [5]) and the visual image information (VIF [6]). No-reference image quality metrics include DIIVINE [7], CBIQ [8], LBIQ [9], BLIINDS [10], BRISQUE [11], and BIQI

[12]. These measures capture deviations from the expected statistics of natural images, where these deviations can be measured in different ways.

1.4 Image denoising methods

Image denoising has been a well-studied problem. The noise is usually assumed to be AWG, whereas the images to be denoised are assumed to contain more structure. This has become the standard setting in image denoising, where the images to be denoised are so-called natural images, or images of every-day scenes. The challenge facing any denoising algorithm is to suppress noise artifacts while retaining finer details and edges in the image. Over the years, researchers have proposed many different methods that attempt to achieve these contradictory goals. These methods vary widely in their approaches. Broadly, these denoising filters can be categorized based on their domain of denoising - spatial or transform domain. Since it is impractical to evaluate the vast number of methods addressing the image denoising problem, we restrict ourselves to a few remarkable ones proposed over years. In Fig.1.2 the state-of–the-art denoising methods are shown by years of their development. The brief survey below is intended to introduce the scope of the research and directions for further development.

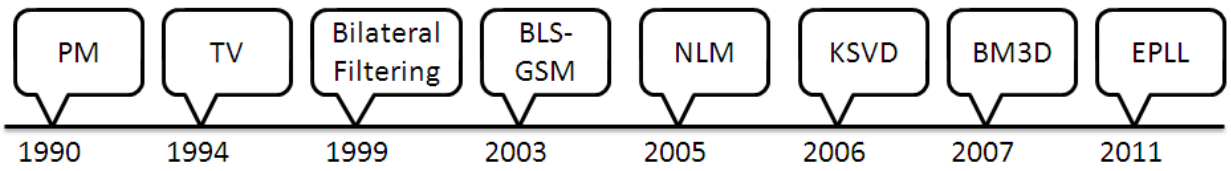

Fig. 1.2. State-of–the-art denoising methods by years of their development

Nonlinear Diffusion:

Nonlinear diffusion has drawn considerable attention over the past decade and has experienced significant developments as it gracefully diffuses the noise in the intra-region while inhibiting inter-region smoothing. Introduced first by Perona and Malik (PM diffusion) [13] the diffusion process is mathematically described by the following equation:

$$\frac{\partial}{\partial t} I(x, y, t) = \nabla \bullet (c(x, y, t) \nabla I) \qquad (2.1),$$

where I(x,y,t) is the image, *t* is the iteration step and *c(x,y,t)* is the diffusion function monotonically decreasing of the magnitude of the image gradient. Two diffusivity functions proposed are:

$$c_1(x, y, t) = \exp\left(-\left(\frac{\left| \nabla I(x, y, t) \right|}{k} \right)^2 \right) \qquad (2.2)$$

and

$$c_2(x, y, t) = \frac{1}{1 + \left(\frac{\left| \nabla I(x, y, t) \right|}{k} \right)^2} \qquad (2.3),$$

where *k* is referred to as a diffusion constant. Depending on the choice of the diffusivity function, equation (2.1) covers a variety of filters. The discrete diffusion structure is translated into the following form:

$$I_{i,j}^{n+1} = I_{i,j}^{n} + (\nabla t) \bullet \begin{bmatrix} c_N \left(\nabla_N I_{i,j}^{n} \right) \bullet \nabla_N I_{i,j}^{n} + c_S \left(\nabla_S I_{i,j}^{n} \right) \bullet \nabla_S I_{i,j}^{n} + \\ c_E \left(\nabla_E I_{i,j}^{n} \right) \bullet \nabla_E I_{i,j}^{n} + c_W \left(\nabla_W I_{i,j}^{n} \right) \bullet \nabla_W I_{i,j}^{n} \end{bmatrix} \qquad (2.4).$$

Subscripts N, S, E and W (North, South, East and West) describe the direction of the local gradient, and the local gradient is calculated using nearest-neighbor differences as

$$\nabla_N I_{i,j} = I_{i-1,j} - I_{i,j};\ \nabla_S I_{i,j} = I_{i+1,j} - I_{i,j}\ \nabla_E I_{i,j} = I_{i,j+1} - I_{i,j};\nabla_W I_{i,j} = I_{i,j-1} - I_{i,j} \quad (2.5).$$

Generally, the effectiveness of the anisotropic diffusion is determined by (a) the efficiency of the edge detection operator to distinguish between noise and edges; (b) the accuracy of an "edge-stopping" function to promote or inhibit diffusion; and (c) the adaptability of a convergence condition to terminate the diffusion process automatically.

Fig. 1.3 Results of nonlinear diffusion for AWGN = 25.

Total variation minimization:

Total variation is a good for quantifying the simplicity of an image since it measures oscillations without unduly punishing discontinuities. For this reason, blocky images reveal very small total variation. In order to recover noisy blocky images Rudin, Osher and Fatemi[14] have proposed to minimize the total variation under constraints which reflect assumptions about noise. This method regards the image denoising problem as a minimization problem. Given a noisy image observation v, the Total Variation

Minimization algorithm try to estimate the original image u via the solution of the following expression:

$$\hat{u}^{TVM} = \arg\min_{u} TV(u)$$

$$TV(u) = \int |\nabla u(x)| dx$$

$$TV(u) = \int \sqrt{u_1^2(x) + u_2^2(x)} dx$$

under the constrains

$$\int (u(x) - v(x)) dx = 0$$

$$\int |u(x) - v(x)|^2 dx = \sigma^2$$

Fig.1.4. Results of TV denoising for AWGN = 25.

By introducing a Lagrange multiplier λ, this minimization problem becomes:

$$\arg\min_{u} TV(u) + \lambda \int |u(x) - v(x)|^2 dx$$

The above function is strictly convex, so that the minimum exits and is computable. In this algorithm, the noise v(x) - u(x) is treated as an error. In practice, some textures are usually presented in the error.

Bilateral Filtering:

Bilateral filter [15] is firstly presented by Tomasi and Manduchi in 1998. The concept of the bilateral filter was also presented in [16] as the SUSAN filter and in [17] as the neighborhood filter. It is mentionable that the Beltrami flow algorithm is considered as the theoretical origin of the bilateral filter [18,19,20], which produces a spectrum of image enhancing algorithms ranging from the l_2 linear diffusion to the l_1 non-linear flows. The bilateral filter takes a weighted sum of the pixels in a local neighborhood; the weights depend on both the spatial distance and the intensity distance. In this way, edges are preserved well while noise is averaged out. Mathematically, at a pixel location x, the output of a bilateral filter is calculated as follows,

$$\tilde{I}(x)=\frac{1}{C}\sum_{y\in N(x)} e^{\frac{-\|y-x\|^2}{2\sigma_d^2}\frac{-|I(y)-I(x)|^2}{2\sigma_r^2}} I(y)$$

where σ_d and σ_r are two hyper-parameters parameters controlling the fall-off of weights in spatial and intensity domains, respectively, N(x) is a spatial neighborhood of pixel I (x) , and C is the normalization constant:

$$C=\sum_{y\in N(x)} e^{\frac{-\|y-x\|^2}{2\sigma_d^2}} e^{\frac{-|I(y)-I(x)|^2}{2\sigma_r^2}}$$

Fig 1.5.: Results of Bilateral Filtering for AWGN = 25.

The optimal value of the hyper-parameters is image-dependent and furthermore depends on the level of noise. However, it is not clear what the relation between the strength of the noise and the optimal hyper-parameter values. In some research, it is shown that the bilateral filter is identical to the first iteration of the Jacobi algorithm (diagonal normalized steepest descent) with a specific cost function. Elad et al. [21] related the bilateral filter with the anisotropic diffusion. However, as is well-known, this filter does not provide effective performance in low signal-to-noise scenarios.

Bayes least square estimate of Gaussian scale mixture (BLS-GSM): The basic idea of this algorithm is modeling a noiseless wavelet coefficient neighborhood, P, by a Gaussian scale mixture (GSM) which is defined as

$$X = \sqrt{z}u$$

where X represents a local cluster of N wavelet neighbor coefficients arranged in a vector, u is a zero-mean Gaussian vector of given covariance, and z is a hidden independent scalar random variable (sometimes termed hidden multiplier, or hidden factor or mixing scale factor) controlling the magnitude of the local response x. The random vector x is termed a Gaussian Scale Mixture (GSM) [22]. It can be interpreted as a continuous infinite mixture of zero-mean Gaussians with the same normalized covariance matrix but with different scale factors (given by $\sqrt{z}$). In the model the choice of u has the same covariance as x, which implies that z has an expected value of 1. Besides the covariance matrix of u, the other feature of the GSM is the mixing density p(z), that tells us the probability of z occurring for every given interval of scale values. The use of "$\sqrt{z}$" in the definition instead of just "z" is chosen because it simplifies the expressions of p(x|z). The GSM's vectors of a given density form hyper-ellipses, and thus GSMs are a particular case of elliptically symmetric distributions.

Let's assume that we have a model, an estimate or a reasonable guess for the mixing density p(z). Then it is easy to demonstrate [23, 24] that the LS solution for estimating the central coefficient of the GSM x vector can be written as:

$$\hat{x}_c = E\{x_c \mid y\} = \int_0^\infty E\{x_c \mid y, z\} p(z \mid y) dz$$

where x_c is the central or reference coefficient of the neighborhood, and $E\{x_c \mid y, z\}$ is the central element of the vector Wiener solution obtained for a particular conditionally Gaussian observation y for a given scale z, assuming the observed sample covariance Cy and zero-mean noise of known covariance C_w:

$$E\{x_c \mid y, z\} = z(C_y - C_w)(z(C_y - C_w) + C_w)^{-1} y$$

This solution is computed, in practice, for a finite (and relatively small - 10, for instance) number of possible z values, converting in practice the continuous GSM into a discrete scale mixture. For every chosen z value they also compute numerically the posteriors p(z|y), for every observed noisy vector y. The latter computation is easy by applying the Bayes rule, given that we know p(y|z), and that we have a model for p(z). The BLS estimation for every central coefficient of every observed neighborhood is just a weighted average of the Wiener solutions according to the probability of each z value given the observed vector y. This strategy provides a smaller quadratic error than the classical (empirical Bayes) approach, which consists of first estimating the hidden variable (z, in this case), and then applying an estimator, as if the estimated value was exact. In such a way the estimate of all the wavelet coefficients of the image are performed and then proceed to reconstruct the image estimate from those coefficients, by inverting the overcomplete wavelet.

Fig.1.6 Results of BLS-GSM for AWGN = 25.

Non-local Means:

The non-local means algorithm, originally proposed in [25] and [26], has stirred a great deal of interest in the community in recent years. At its core, however, it is a relatively simple generalization of the bilateral filter; namely, the photometric term in the bilateral similarity kernel, which is measured point-wise, is simply replaced with one that is patch-wise. A second difference is that the geometric distance between the patches (corresponding to the first term in the bilateral similarity kernel), is essentially ignored, leading to strong contribution from patches that may not be physically near the pixel of interest (hence the name non-local). To summarize, the NLM kernel is

$$K(x_i, x_j, y_i, y_j) = \exp\left(\frac{-\|x_i - x_j\|^2}{h_x^2}\right)\exp\left(\frac{-\|y_i - y_j\|^2}{h_y^2}\right) \quad with \;\; h_x \to \infty$$

where y_i and y_j refer now to patches of pixels centered at pixels y_i and y_j, respectively.

Fig.1.7 Results using NLM for AWGN = 25.

In practice, two implementation details should be observed. First, the patch-wise photometric distance $\| y_i - y_j \|^2$ in the above is in fact measured as $(y_i - y_j)^T G(y_i - y_j)$ where G is a fixed diagonal matrix containing Gaussian weights which give higher importance to the center of the respective patches. Second, it is computationally rather impractical to compare all the patches y_i to y_j , so although the non-local means approach in Buades et al. [25] theoretically forces h_x to be infinite, in practice typically the search is limited to a reasonable spatial neighborhood of y_j . Consequently, in effect the NLM filter too is more or less local; or said another way, h_x is never infinite in practice. The method in Awate et al. [26], on the other hand, proposes a Gaussian-distributed sample which comes closer to the exponential weighting on Euclidean distances in the above equation.

KSVD:

The K-SVD method was introduced in [27] where the whole objective was to optimize the quality of sparse approximations of vectors in a learnt dictionary. The kernel regression-based framework typically employs an implicit local model of the image for denoising, many spatial-domain methods employ a more explicit model-based approach. In most of these methods the models act as prior information about the clean image and are either learned a priori from noise-free natural images or directly from the noisy image. Denoising is then performed by enforcing these priors on the noisy image. One of the most popular model-based methods is the K-SVD algorithm [27]. There the authors propose a patch-based framework where each patch in the image is represented as a linear combination of patches from some over-complete set of bases. Building on the

observation that noise-free image patches are sparse-representable [], the authors enforce a constraint on the number of basis patches (or atoms) that can be used in estimating any given patch. Mathematically, the problem can be formulated as

$$\hat{z}_i = \Phi\hat{\beta}_i, \ \textit{where}$$

$$\hat{\beta}_i = \arg\min_{\beta_i} \left\| y_i - \Phi\hat{\beta}_i \right\|^2 \text{ subject to } \left\| \beta_i \right\|_0 \leq \tau$$

Fig.1.8 Results using KSVD for AWGN = 25.

Learning from the noisy image: KSVD [27] is an iterative algorithm that learns a dictionary on the noisy image at hand. An iteration of the algorithm consists of the following two steps:

1. Find the coefficients for each patch in the image

2. Update the dictionary, one column at a time.

Usually 10 iterations are sufficient to achieve good results. The step updating the dictionary relies on an SVD-decomposition, hence the name of the algorithm. Dictionaries learned in such a way often contain features also present in the image on which the dictionary was learned.

K Locally Learned Dictionaries (KLLD):

As against learning a single overcomplete dictionary for the entire image, the authors of the KLLD (K locally learned dictionaries) approach [28] perform a clustering step using K-Means on (coarsely pre-filtered) patches from the noisy image and then filter the patches from each cluster separately by projecting them onto lower-rank bases (learned by PCA) coupled with a kernel regression framework from [29]. The entire procedure is iterated for better performance. This scheme works well for medium or low noise levels. However, the clustering is not very reliable at high noise levels due to the fact that weights of steering kernel regression are vulnerable to severe noise. The generally flow of KLLD is described in Figure

Block Matching and 3D filtering (*BM3D):*

BM3D is the abbreviation of Block Matching and 3D filtering [30], which is a brilliant work of Dabov, et al from Tampere University of Technology, Finland. It is commonly regarded as the state-of-the-art real-time denoisng algorithm. The main idea is based on an enhanced sparse representation of image blocks in transform-domain. The enhancement of the sparsity is achieved by grouping similar 2D image fragments (e.g.

blocks) into 3D data arrays. Then collaborative filtering is applied to deal with these 3D groups.

Figure 1.9 Results using KLLD for AWGN = 25.

The collaborative filtering is achieved by three successive steps: 3D transformation of 3D group, shrinkage of transform spectrum, and inverse 3D transformation. The result is a 3D estimate that consists of the jointly filtered grouped image blocks. By attenuating the noise, the collaborative filtering reveals the details shared by grouped blocks. And the filtered blocks are then returned to their original positions. Because the blocks are overlapping, for each pixel we can obtain many different estimates which need to be combined. Aggregation scheme is then exploited to take advantage of this redundancy.

Specifically, in Step1 first apply a basic estimation to find blocks that are similar with the current block and form a 3D group together. Then we apply a separable 3D transform on the 3D group. The separable 3D transform is composed by a basic 2D transform and a 1D

Haar transform on the third dimension. Finally, a primary estimate of the original image is obtained by aggregation. Aggregation is performed by a weighted averaging at those pixels positions where there are overlapping block-wise estimates.

In Step 2, similarly grouping and 3D collaborative filtering are applied to both the primary estimate and the noisy image. The different in this step is the 3D filtering in Step2 makes use of the energy spectrum of the primary estimate obtained in Step1. So we can apply DCT and Haar-wavelet Wiener filtering to get the final estimate of u.

The final estimate output is obtained by aggregation:

$$\hat{u}^{final} = \frac{\sum_x w_x \cdot \hat{u}_x^{wiener}}{\sum_x w_x}$$

where $\hat{u}_x^{wiener}$ is the estimated estimate of each image block in different block groups via collaborative filter.

Fig.1.10 Results using BM3D for AWGN = 25.

Denoising an image of size 512 x 512 takes on the order of 5 seconds on a modern computer. The method often achieves outstanding results and is considered state-of-the-art.

Expected Patch Log Likelihood (EPLL):

Many denoising methods denoise image patches independently and apply averaging or other similar techniques in areas of overlapping patches. Dictionary denoising method such as KSVD [27] are examples of such methods. The problem with this approach is that the averaging process can create patches in the denoised images that do not look good. EPLL [31] is an acronym from expected patch log likelihood. The method contrasts itself from methods that denoise patches independently by aiming at creating a denoised image in which each patch is likely under a given patch prior, while staying close to the noisy image. EPLL takes a maximum a posteriori (MAP) approach to denoising: Given an image corrupted with AWG noise y = x + n, we want to find $\hat{x}$:

$$\hat{x} = \arg\max_x p(x \mid y)$$

$$\hat{x} = \arg\max_x p(y \mid x)p(x)$$

$$\hat{x} = \arg\min_x -\log(p(y \mid x)) - \log(p(x))$$

$$\hat{x} = \arg\min_x -\log\frac{\lambda}{2}\|x-y\|^2 - EPLL(x),$$

where λ controls the trade-of between the prior and the data fidelity term, as usual in MAP estimation. The expected patch log-likelihood (EPLL) is defined as:

$$EPLL(x) = \sum_i \log(p(P_i x)),$$

where P_i extracts patch i out of an image. The EPLL is therefore the sum over the expected patch log-likelihoods of all sliding window patches in an image. The EPLL is not the expected log-likelihood of a full image. Optimization is performed using half-quadratic splitting, which introduces auxiliary variables and alternates between two steps: (i) updating the auxiliary variables while keeping the image patches fixed, and (ii) updating the image patches while keeping the auxiliary variables fixed. This procedure is repeated for a small number of iterations.

We see that the method does not depend on a specific image prior: In principle, any probabilistic patch prior could be used. An advantage of the method is that one need not learn a prior on entire natural images, as other methods such as Fields of Experts attempt to do. Instead, one need only learn a prior on natural image patches, which is considerably easier. Though the method can theoretically use any probabilistic patch prior, the best results achieved in the paper are obtained using a Gaussian mixture model (GMM):

$$\log p(x) = \log \sum_{k=1}^{K} \pi_k N(x \mid \mu_k, \Sigma_k).$$

The results described in the paper are comparable to those achieved with other state-of the-art methods such as BM3D.

Denoising methods follow one of the following two paradigms:

1. Focus on images: Methods making simple assumptions about the noise, and focusing instead on the properties of images.

2. Focus on noise: Methods making simple assumptions about images, and focusing instead on the properties of the noise.

The visual image quality after non-linear diffusion could be poor because of the removal of the textures and contours and the denoising performance is greatly constrained by the error propagation when the noise variance becomes large. BLS-GSM and KLLD suffer from strong Gibbs effect near all image boundaries. This Gibbs effect is nearly not noticeable in the image denoised by K-SVD, since the use of the whole dictionary permits to better reconstruct edges when the right atoms are present in the dictionary. The NL-means denoised image has no visual artifacts but is more blurred than those given by BM3D. The BM3D denoised images has some Gibbs effect near edges. The visual and subjective quality of BM3D however have a superior performance to the rest of the methods.

1.5 Research objectives, tasks, and contribution of this work

Across a number of described methods, the noise is usually assumed to be AWG, whereas the images to be denoised are assumed to contain more structure. This has become the standard setting in the image denoising, wherein the images to be denoised are so-called natural images, or images of every-day scenes. This is a classical image denoising problem which does not take into account a specific imagery or noise. The knowledge-based methods constitute the state-of-the art in denoising. In their core, they look for regions within an image that are similar in appearance for deriving a better statistics for denoising. A simple example of that is the NL-means [25, 26]. It looks for similar patches within a given noisy image and calculates a weighted average of the center pixels. BM3D [30] also exploits the idea of grouping patches that are similar in appearance, but performs denoising on the group of patches in the transform domain.

Among advanced denoising methods nonlinear diffusion with its iterative procedure of quality optimization and the gradient-based pixel diffusion is powerful in view of edge preservation capability without producing ringing artifacts in the filtered images. These filters perform time evolutionary processes, in which the denoised image is a solution of a diffusion equation modeled as a PDE with spatially varying diffusion coefficients. Since the introduction of the first nonlinear diffusion filter by Perona and Malik [13] in 1990, enhancing the performance of the PDE-based nonlinear diffusion further has been a subject of many research efforts. In these improved techniques, the focus has been on introducing new or modified diffusivity functions providing better control of the diffusion process.

The PDE modeling of the nonlinear diffusion process invariably makes use of kernels to approximate time and spatial rate of change of the image intensities. It should be noted that the kernels themselves have impact on the characteristics of the diffusing images. This impact of the kernels needs to be studied in the context of noise removal and edge preservation capabilities of the nonlinear diffusion process.

In nonlinear diffusion filters a diffusivity function is used to control the diffusion process. In order to provide a good control of the noise diffusion and edge preservation, such a function should be a function of image gradient as well as image intensities. With a proper choice of this model, the rate of diffusion at edge pixels is made different from that at non-edge pixels.

The nonlinear diffusion methods can be augmented in their edge/structure preservation ability using one or more of the following approaches:

a) Adaptation to the local structure

b) A better edge/structure estimate (better than the gradient estimate) for different noise levels.

c) Diffusion in the transform domain (iterative shrinkage).

In this work, a study is undertaken to enhance the performance of non-linear diffusion first by introducing new diffusivity functions. Further, we investigate the impact of local adaptation. Based on this study, a structure-adaptive nonlinear diffusion is designed with a view to providing filters with a better edge preservation capability while removing the noise effectively in intensity domain. Also, the wavelet domain diffusion is explored as an extension of the shrinkage process, and a method is designed to diffuse wavelet coefficients based on the context information. Finally, a systematic study is of adaptation of the diffusion process within image patches. The studies are finalized with the development of a high performance method which combines feature- and patch-based adaptation of diffusion. Throughout the dissertation, we use PSNR and UIQI as metrics for comparison and performance reporting. The PSNR is a statistical method of estimating differences between samples based on per pixel comparison. It is widely used by the industry and academia for its simplicity in the quality assessment. However, because it's based on computing pixel differences, PSNR fails to capture structured or localized errors; and it also cannot differentiate between different types of errors (errors with different impact on a human observer can have the same PSNR). UIQI is a more complex metric based on properties of the Human Visual System (HVS) that is starting to replace PSNR as the most widely used metric because of it is independent of viewing conditions and individual observers. This quality index models any distortion as a

combination of three different factors: loss of correlation, luminance distortion, and contrast distortion, and thus is concerned with more disturbing factors than PSNR solely.

1.6 Organization of the Dissertation

In Chapter 2, a brief account of the development of the Perona-Malik nonlinear diffusion filter is given. The development begins with a premise that image diffusion is a process satisfying the scale-space properties and ends with a nonlinear PDE model for the process of image diffusion. Two models of the Perona-Malik filter, each emphasizing a different strategy for noise diffusion and edge preservation are discussed. This chapter serves as a platform for further development of the ideas undertaken in this work.

In Chapter 3 the application of robust m-estimators as a diffusivity functions is discussed. Based on this study, the new m-estimators weight functions are incorporated into the nonlinear diffusion filters to demonstrate their effectiveness.

In Chapter 4, the role of textons is investigated. A novel local binary pattern (LBP) [32] based adaptive diffusion is presented. The LBP operator unifies traditionally divergent statistical and structural models of region analysis. We use LBP textons to classify an image around a pixel into noisy, homogenous, corner and edge regions. According to different types of regions, a variable weight is assigned in to the diffusion equation, so that our algorithm can adaptively encourage strong diffusion in homogenous/ noisy regions and less on the edge/ corner regions.

In Chapter 5, the role of nonlinear diffusion in wavelet domain with the adaption to local context is investigated. We propose a context adaptive nonlinear diffusion method, which we called SWCD, for image denoising in wavelet domain. In diffusing detail

coefficients of stationary wavelet transform (SWT), the local context is taken into account such that strong edges, i.e. high magnitudes of details coefficients due to the object or textures are diffused in a lesser amounts and smooth regions of images characterized by “valleys” of low magnitude coefficients are diffused in a greater extent. The local context which is derived directly through the distribution of transform energies across the scales 1 and 2 of two-level SWT provide the context information and control the diffusion. The shift invariance of SWT contributes to the performance of the method.

In Chapter 6 a novel locally- and feature-adaptive diffusion based method for denoising is presented. The method approaches each image patch/region individually and uses a different number of diffusion iterations per region to attain the best objective quality according to the PSNR metric. Unlike block-transform based methods, which perform with a pre-determined block size, and clustering-based denoising methods, which use a fixed number of classes, the proposed method searches for an optimum patch size through an iterative diffusion process. It is initialized with a small patch size and proceeds with aggregation of patches until the best PSNR value is attained. In the diffusion model the gradient value, is replaced by Inverse Difference Moment (IDM) [33], which is shown to be a robust feature in determining the amount of local intensity variation in the presence of noise.

Finally, Chapter 7 summarizes the work of the study undertaken in this dissertation and highlights its contributions. Some suggestions for the future work based on the ideas and schemes developed in this dissertation are also given.

CHAPTER 2

LITERATURE REVIEW

Diffusion based methods appear in a large variety of image processing areas ranging from image restoration, post-processing fluctuating data, texture segmentation, image sequence analysis, edge detection. In the previous Chapter we have shown that not all the possibilities of the diffusion based de-noising have been explored. This chapter reviews the main application, namely image restoration using diffusion. It is written in an informal style and refers to a large amount of original literature, where proof and full mathematical details can be found.

The goal is to give an introduction to the theoretical framework in which our adaptive nonlinear diffusion is developed. On the one hand, this should make the reader sensitive to the similarities, differences and problems of all these methods, on the other hand it shows how our work relates to them and motivates the reader to study how some of the these problems will be solved later on.

The outline of this chapter is as follows: we start with reviewing the ideas behind diffusion processes. This helps us to understand the next sections which are connected with the properties of linear and nonlinear diffusion filters in image processing. The last section summarizes the shortcomings of the core methods and gives an outline of the questions we are concerned with in the subsequent chapters.

2.1 Linear Filters

Linear filters are the simplest kind of diffusion filters available. They apply the same amount of filtering or diffusion to every pixel of data. So we get a data independent blurring of the signal.

Gaussian smoothing

A widely use way to smooth a signal represented by a real-valued mapping $u \in L^1(R^2)$ is a convolution with Gaussian kernel

$$(G_\sigma * u)(x) = \int_{R^2} G_\sigma(x-y)u(y)dy$$

G_σ represents the two-dimensional Gaussian with width (standard deviation) $\sigma = \sqrt{2t} > 0$ which read as

$$G_\sigma(x) = \frac{1}{2\Pi\sigma^2}\exp\left(-\frac{|x|^2}{2\sigma^2}\right)$$

$$= \frac{1}{4\Pi t}\exp\left(-\frac{|x|^2}{4t}\right)$$

$$= G(t,x)$$

From the convolution theorem it follows that the Fourier transform of the convolution is equal to the product of the Fourier transform of the convolution kernel and the function u, i.e.

$$F[G_\sigma * u](\omega) = F[G_\sigma](\omega)\cdot F[u](\omega)$$

With the fourier transform defined by

$$F[u](\omega) = \int_{R^2} u(x)\exp(-i\langle\omega, x\rangle)dx$$

The interesting, but not astonishing fact is that the fourier transform of a gaussain shaped function is again of Gaussian form:

$$F[G_\sigma](\omega) = \exp\left(-\frac{(|\omega|\sigma)^2}{2}\right)$$

Thus, it follows that

$$F[G_\sigma * u](\omega) = \exp\left(-\frac{(|\omega|\sigma)^2}{2}\right) F[u](\omega)$$

i.e. the convolution with a Gaussian is low-pass filter that inhibits frequencies (oscillations in the space domain). This damping of high frequencies in the signal u in a monotone way can be viewed as a diffusion process.

2.2 Linear diffusion equations

It is easy to see that the convolution of a signal u with a Gaussian kernel G_σ is a smoothing process. Since G_σ is a mollifier, high frequencies are damped and the total variation of the signal u is reduced. If we look at the smoothed signal

$$u_\sigma(x) = \int_{R^2} G_\sigma(x-y)u(y)dy$$

from the theory for linear partial differential equations we have the following. The solution of the linear heat equation

$$\partial_t u = \Delta u$$
$$u(0,x) = u_0(x)$$

With bounded initial data $u_0(x) \in C(R^2)$ is given by

$$u(t,x) = u_{\sigma^n}(x)$$

$$= \int_{R^2} G_\sigma(x-y)u(t,y)dy$$

From this well-known fact one immediately sees that linear filtering of a signal u by convolution is equivalent to solving the linear heat equation for the initial data u_0. If we restrict ourselves for a moment to one space dimension and look for a suitable discrete approximation of the heat equation, we see that the finite difference formulation

$$\frac{u(t^{n+1},x_i)-u(t^n,x_i)}{\Delta t} = \frac{u(t,x+h)-2u(t,x)+u(t,x-h)}{h^2}$$

A time advancing scheme for the solution of the heat equation consequently reads as

$$U^i = U_i + \frac{\Delta t}{h^2}\left[U_{i+1} - 2U_i + U_{i-1}\right],$$

which is the simplest discrete model for a low pass filter.

2.3 Nonlinear diffusion filters

As we have already seen linear diffusion filters are a very effective way to extract or reduce high frequency oscillations from a signal. However, due to their linearity the tendency to blur the signal is quite strong and leads to a smoothing of the gradients like edges, steps or corners which are intended to be enhanced or recovered. This results in shape distortions, since smoothing over object boundaries can affect its shape and localization of the edge. Therefore, there is a need to control the smoothing process via nonlinear and adaptive control of the diffusion filtering. This should be based on local properties of the signal in order to control the strength of the dissipation. The first formulation of such a nonlinear diffusion filter in image processing was given by Perona and Malik [13].

The basic idea is to modify the conductivity in the nonlinear diffusion equation

$$\frac{\partial}{\partial t} I(x, y, t) = \nabla \bullet (c(x, y, t) \nabla I) \qquad (1),$$

where *I(x,y,t)* is an image, *t* is the iteration step and *c(x,y,t)* is the monotonically decreasing function of the image gradient called diffusion function. Two diffusivity functions that have been proposed are:

$$c_1(x, y, t) = \exp\left(-\left(\frac{|\nabla I(x, y, t)|}{\lambda} \right)^2 \right) \qquad (2)$$

and

$$c_2(x, y, t) = \frac{1}{1 + \left(\frac{|\nabla I(x, y, t)|}{\lambda} \right)^2} \qquad (3),$$

where λ is referred to as the diffusion constant. Depending on the choice of the diffusivity function, Equation (1) covers a variety of filters. The previously employed diffusivity functions:

i. Linear diffusivity : $c(x, y, t) = 1$

ii. Charbonnier diffusivity : $c(x, y, t) = \frac{1}{\sqrt{1 + \left(\frac{|\nabla I(x, y, t)|}{\lambda} \right)^2}}$

iii. Perona–Malik diffusivity 1: $c(x, y, t) = \frac{1}{1 + \left(\frac{|\nabla I(x, y, t)|}{\lambda} \right)^2}$

iv. Perona–Malik diffusivity 2 : $c(x,y,t) = \exp\left(-\left(\frac{|\nabla I(x,y,t)|}{\lambda}\right)^2\right)$

v. Weickert diffusivity :

$$c(x,y,t) = \begin{cases} 1 & |\nabla I(x,y,t)| = 0 \\ 1 - \exp\left(\frac{-3.3148}{\left(\frac{|\nabla I(x,y,t)|}{\lambda}\right)^2}\right) & |\nabla I(x,y,t)| > 0 \end{cases}$$

vi. TV diffusivity : $c(x,y,t) = \frac{1}{|\nabla I(x,y,t)|}$

vii. BFB diffusivity : $c(x,y,t) = \frac{1}{|\nabla I(x,y,t)|^2}$

viii. FAB diffusivity : $c(x,y,t) = 2\exp\left(-\left(\frac{|\nabla I(x,y,t)|}{\lambda 1}\right)^2\right) - \exp\left(-\left(\frac{|\nabla I(x,y,t)|}{\lambda 2}\right)^2\right) \quad \lambda 1 < \lambda 2$

The diffusivities i–v are bounded from above by 1, while the diffusivities vi and vii are unbounded. The forward and backward (FAB) diffusivity viii differs from the other diffusivities by the fact that it may even attain negative values. Well posedness results are available for the diffusivities i, ii and vi, since they result from convex potentials. For the diffusivities iii, iv and v which can be related to nonconvex potentials, some well posedness questions are open in the continuous setting, while already a space discretization creates well posed processes. The FAB diffusivity viii goes one step further by allowing even negative values. However, at extrema the FAB diffusivity is in the forward diffusion region which is responsible for a certain degree of stability.

The discrete diffusion structure is translated into the following form:

$$I_{i,j}^{n+1} = I_{i,j}^{n} + (\nabla t) \bullet \begin{bmatrix} c_N\left(\nabla_N I_{i,j}^{n}\right) \bullet \nabla_N I_{i,j}^{n} + c_S\left(\nabla_S I_{i,j}^{n}\right) \bullet \nabla_S I_{i,j}^{n} + \\ c_E\left(\nabla_E I_{i,j}^{n}\right) \bullet \nabla_E I_{i,j}^{n} + c_W\left(\nabla_W I_{i,j}^{n}\right) \bullet \nabla_W I_{i,j}^{n} \end{bmatrix} \quad (4).$$

Subscripts N, S, E, and W (North, South, East, and West) describe the direction of the local gradient, and the local gradient is calculated using nearest-neighbor differences as

$$\nabla_N I_{i,j} = I_{i-1,j} - I_{i,j}; \quad \nabla_S I_{i,j} = I_{i+1,j} - I_{i,j} \; \nabla_E I_{i,j} = I_{i,j+1} - I_{i,j}; \nabla_W I_{i,j} = I_{i,j-1} - I_{i,j} \quad (5).$$

The model in [13] has several practical and theoretical limits. It needs a reliable estimate of image gradients because with an increase in noise level, the effectiveness of the gradient calculation degrades and thus deteriorates the performance of the method. Furthermore, an equal number of iterations in the diffusion of all pixels in the image lead to blurring of textures and fine edges while the smooth regions benefit. Fig.2.1-2.3 shows the results of PM application results for different noise levels σ =10, 20, 50 and 100.

Fig.2.1 First row: "Lena" image and that with AWG noise, σ =10, 20, 50 and 100; Second row: Corresponding results of PM.

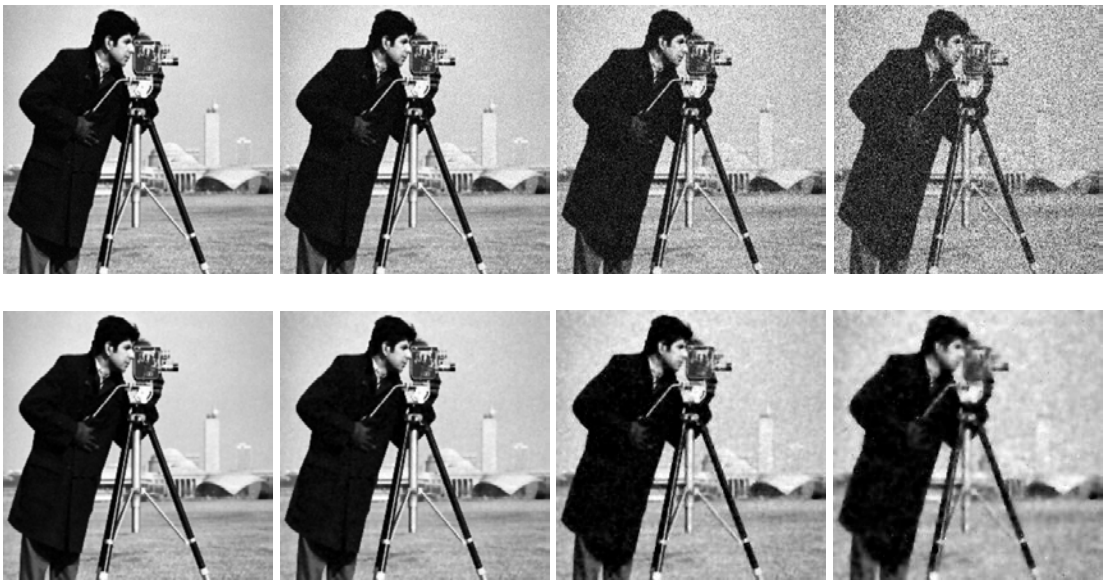

Fig.2.2 First row: “Cameraman” image and that with AWG noise, σ =10, 20, 50 and 100; Second row: Corresponding results of PM.

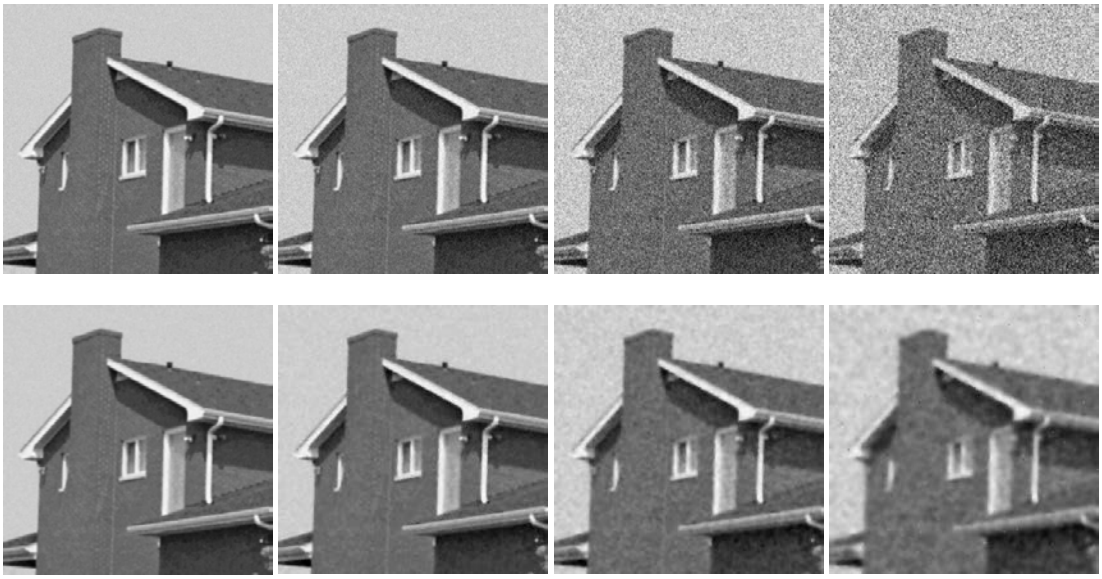

Fig.2.3 First row: “House” image and that with AWG noise, σ =10, 20, 50 and 100; Second row: Corresponding results of PM.

The most commonly functions used for noise removal and image enhancement are PM [13] and Weickert’s diffusivity functions (WF) [40, 41]. The PM filter works better on

smooth regions while the WF does preserves the boundaries between different regions. In this section we will see how both functions work on smooth and texture regions. For demonstration, let us apply PM and WF to complete image of “Lena”. Fig.2.4 and 2.5 shows the results of PM and WF on “Lena” image for noise levels σ =20 and 50 respectively. We can observe that WF based diffusion creates artifacts. Fig.2.6 and 2.7 shows the results of PM and WF on smooth regions for noise levels σ =20 and 50. From the results we conclude that PM performs better on smooth regions while the WF creates artifacts. Fig.2.8 and 2.9 shows the results of the PM and the WF on texture regions for noise levels σ =20 and 50. One can see that PM performs much better compared to the WF results on texture regions; the artifacts are visible.

There is clear indication of that PM works better in the local patches compared to that of the WF. For further demonstration, let us apply PM diffusion to two different image patches, each representing a certain structural content, e.g., a texture and a smooth region. Fig. 2.10 indicates significant differences in PSNR values versus iteration numbers for the provided examples. The examples in Fig. 2.11 show how image quality changes between iterations 22 and 30. In the left image, pixels are corrupted in a smooth region, and in the right, details are severely blurred.

Generally, the effectiveness of the anisotropic diffusion is determined by (a) the efficiency of the edge detection operator to distinguish between noise and edges; (b) the accuracy of an “edge-stopping” function to promote or inhibit diffusion; and (c) the adaptability of a convergence condition to terminate the diffusion process automatically. Research on diffusion-based denoising targets one or more of the above factors.

Fig.2.4 First row: “Lena” image and that with AWG noise, σ =20 and 50;
Second row: Corresponding results of PM.

Fig.2.5 First row: “Lena” image and that with AWG noise, σ =20 and 50;
Second row: Corresponding results of WF diffusion.

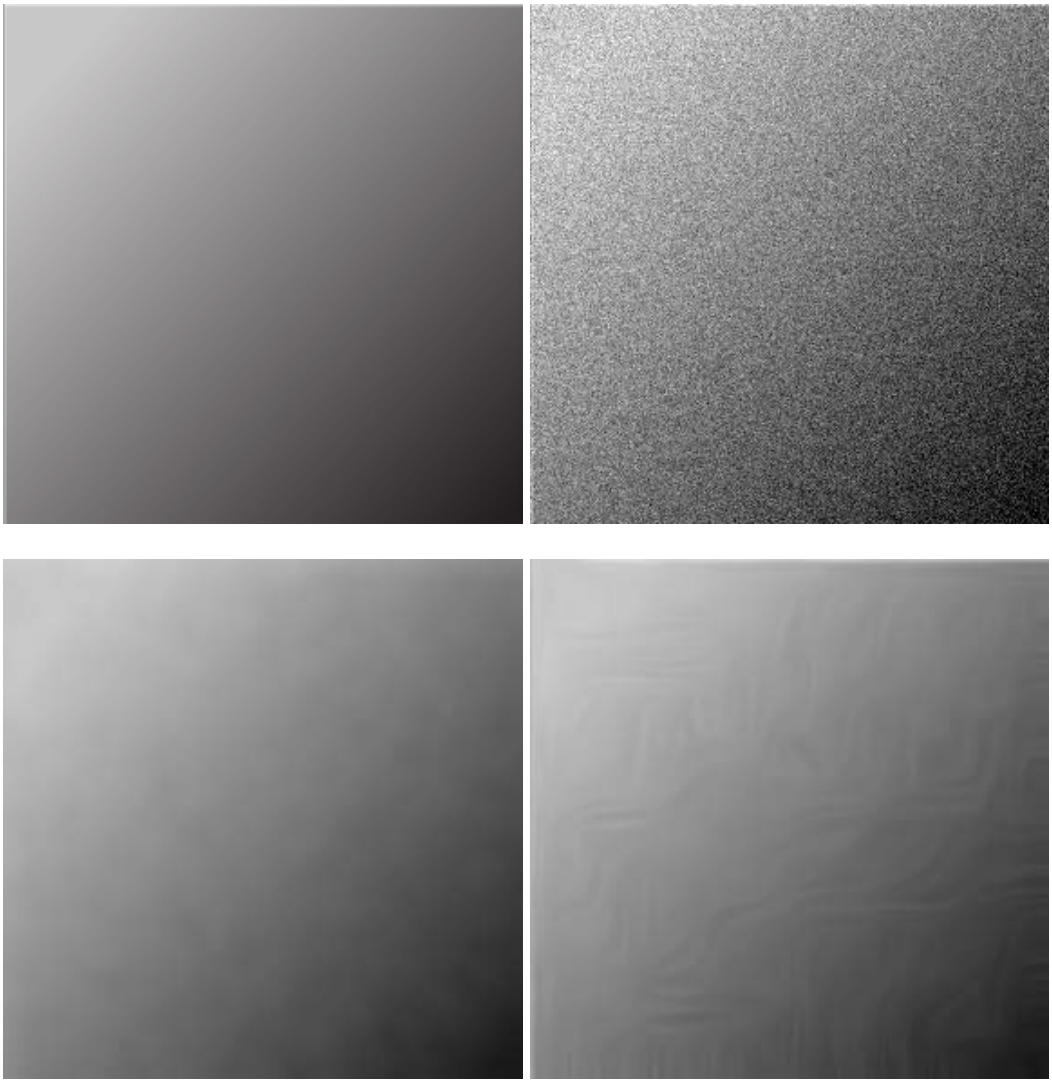

Fig.2.6 First row: “Smooth” image and that with AWG noise, σ =20;
Second row: Corresponding results of PM and WF diffusion.

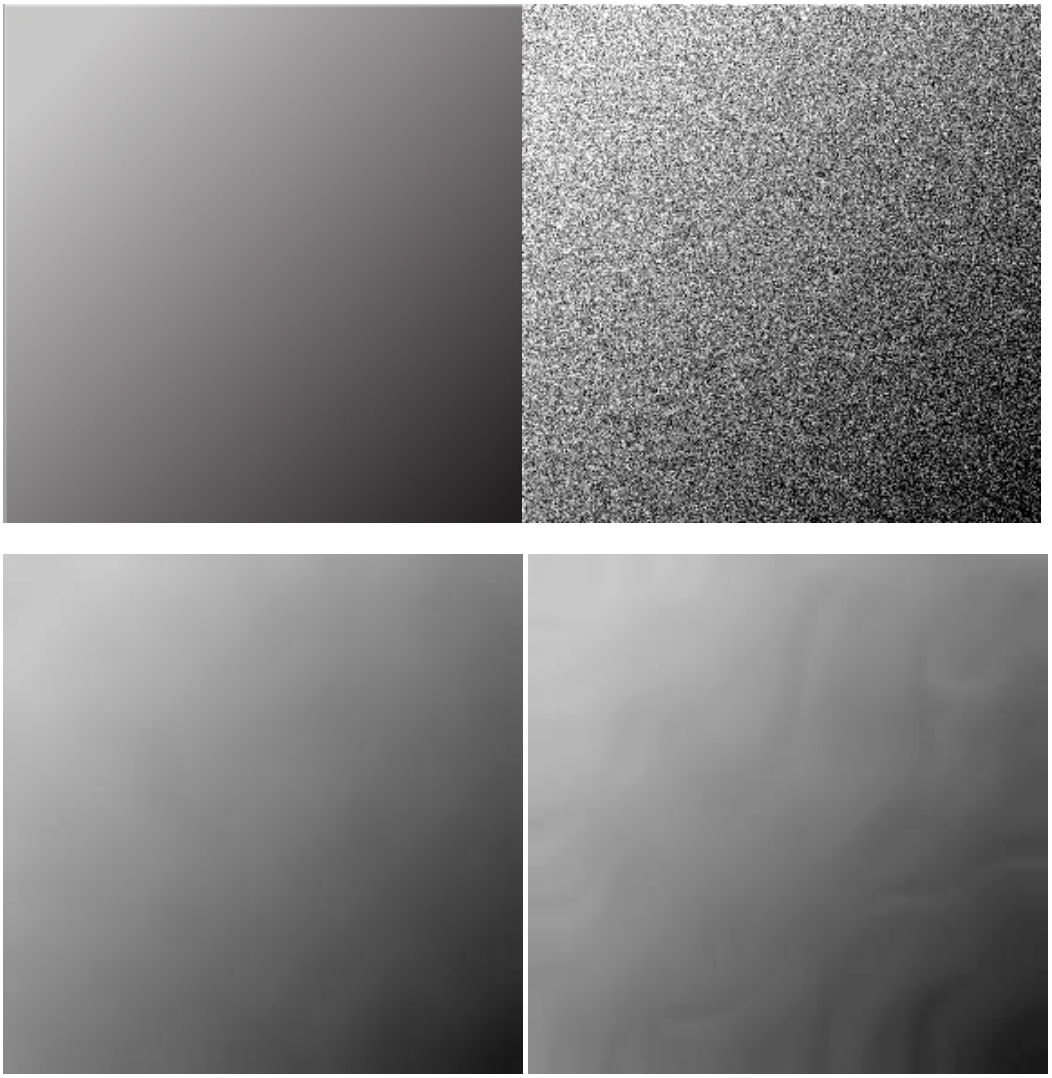

Fig.2.7 First row: “Smooth” image and that with AWG noise, σ =50;
Second row: Corresponding results of PM and WF diffusion.

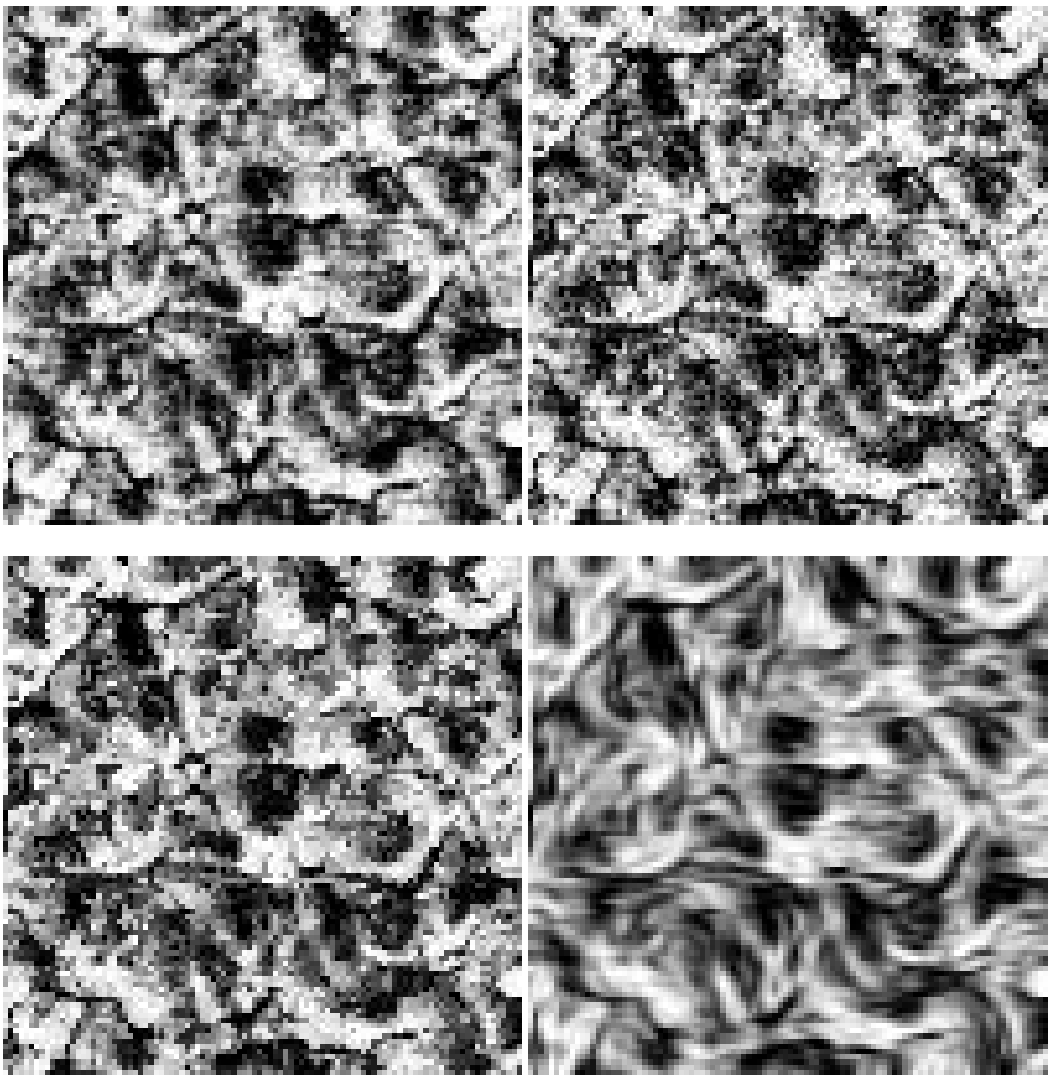

Fig.2.8 First row: “texture” image and that with AWG noise, σ =20;
Second row: Corresponding results of PM and WF diffusion.

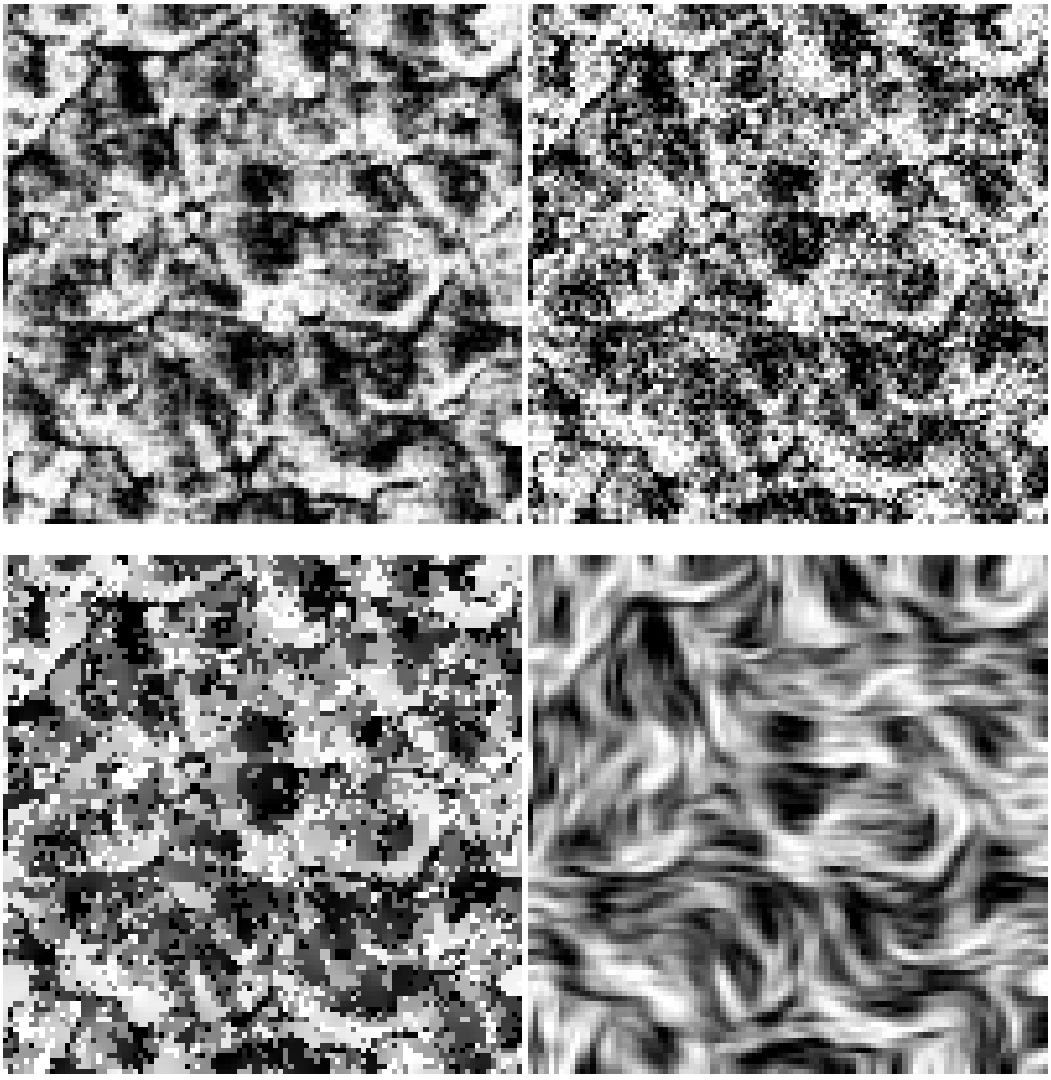

Fig.2.9 First row: “texture” image and that with AWG noise, σ =50;

Second row: Corresponding results of PM and WF diffusion.

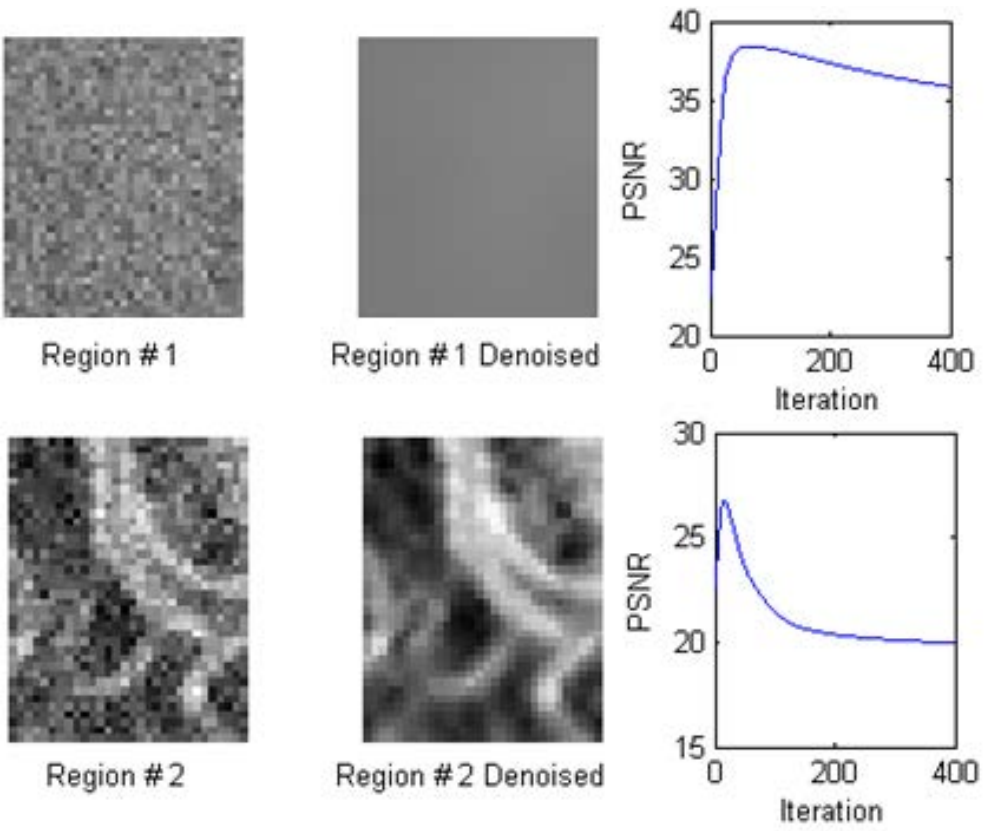

Fig. 2.10. Denoising results for two different structural contents.

Fig. 2.11 PM denoised "Lena" image for two different iteration numbers (left = 22 iterations, PSNR = 29.37 dB; right = 30 iterations, PSNR = 28.52 dB) for AWG noise level, σ =20.

Catte et al. [42] used a smoothed gradient of the image, rather than the true gradient. Let G_σ be a smoothing kernel; then

$$\frac{\partial}{\partial t} I(x, y, t) = \nabla \bullet (c(\|\nabla G_\sigma * I\|)\nabla I)$$

.

The smoothing operator removes some of the noise that might have deceived the original PM filter. In this case, the scale parameter σ is fixed. In [43], the authors have proposed inhomogeneous anisotropic diffusion that includes separate multiscale edge detection.

Yu et al. [44] have incorporated the SUSAN edge detector into the model:

$$\frac{\partial}{\partial t} I(x, y, t) = \nabla \bullet (SUSAN(c(\|\nabla G_\sigma * I\|))\nabla I)$$

Due to noise suppression, the SUSAN can guide the diffusion process in an effective manner. Li et al. [45] proposed a context-adaptive anisotropic diffusion via a weighted diffusivity function. It is represented by the equation

$$\frac{\partial}{\partial t} I(x, y, t) = \nabla \bullet (w(x, y, t)c(x, y, t)\nabla I),$$

where the combined term *w(x,y,t)c(x,y,t)* is referred to as the weighted diffusivity function and *w(x,y,t)* is a pixel-wise feature dependent weight function.

Chao and Tsai [46] proposed a diffusion model which incorporates both the local gradient and gray-level variance. High levels of noise produce larger magnitudes of variance and gradients than those by objects and textures. Thus, the method becomes inefficient for high noise levels. Wang et al. [47] studied a local variance controlled scheme wherein the spatial gradient and contextual discontinuity of a pixel are jointly employed to control the evolution. However, a solution to estimating the contextual discontinuity requires an exhaustive search procedure, which causes the algorithm to be

too computationally expensive. Yu and Acton [48] proposed speckle-reducing anisotropic diffusion (SRAD), which integrated spatially adaptive filters into the diffusion and provided considerable improvement in speckle suppression over other conventional diffusion methods. Abd-Elmoniem et al. [49] devised a coherence-enhancing nonlinear coherent diffusion (CENCD) model for speckle reduction. This method combines isotropic diffusion, anisotropic coherent diffusion, and mean curvature motion. The aim is to maximally filter those regions which correspond to fully developed speckle while preserving information associated with object structures. Zhang et al. [50] presented a Laplacian pyramid-based nonlinear diffusion (LPND) method where a Laplacian pyramid was utilized as a multiscale analysis tool to decompose an image into sub-bands. Then, anisotropic diffusion of a variable flux is applied to different subbands was used to suppress noise in each sub-band. LPND tries to introduce sparsity and multiresolution properties of multiscale analysis into anisotropic diffusion.

Recent work [51, 52, 53, 36, 54, 55, 56 and 57] has shown that nonlinear anisotropic diffusion can be employed within the framework of the discrete wavelet transform. Mrazek et al. [36] have analyzed correspondences between explicit one-dimensional schemes for nonlinear diffusion and discrete translation-invariant Haar wavelet shrinkage. Weickert et al. [36, 55] described relation between (semi-)discrete diffusion filtering and Haar wavelet shrinkage, including an analytic four-pixel scheme, but focused on the 1-D or the isotropic 2-D case with a scalar-valued diffusivity. This allowed to enhancing edges compared to Perona-Malik diffusion [13].

Shih and Liao [54] addressed a single step nonlinear diffusion that can be considered equivalent to a single shrinkage iteration of coefficients of Mallat’s Zhong

dyadic wavelet transform (MZ-DWT) [58]. Nonlinear diffusion begins with a gradient operator, which may be badly influenced by the noise present in the image. MZ-DWT has its own subband filtering framework and a set of wavelet filters, derived from the derivative of a smoothing function. Diffusion is directly performed on coefficients of horizontal and vertical subbands and has shown improvements compared to WF diffusion[60,61].

In [56] authors presented a nonlinear multiscale wavelet diffusion method for the ultrasound speckle suppression and edge enhancement. The edges are detected using normalized wavelet modulus and speckle is suppressed by an iterative multiscale diffusion of wavelet coefficients. The diffusion threshold is estimated from the normalized modulus in the homogenous speckle regions, in order to adapt to the noise variation with iteration. The automatic identification of homogenous regions is implemented using two-stage classification. First, the normalized modulus at each scale is classified using the likelihood method based on the Rayleigh mixture model. Second, the homogenous speckle region is identified by a coarse-to-fine classification utilizing the edge persistence across scales. In this procedure, a tuning parameter is introduced to adjust the diffusion threshold, and it further controls the final denoising result. Although the method was able to reduce the speckle and preserve edges, it was observed that the low-contrast edges are blurred significantly. Furthermore the parameters are selected manually for a type of details desired to be addressed. To remove the speckle noise, the texture details are also victimized. Overall the application of the method limited to ultrasound image application.

In [52], Bruni et al. proposed another wavelet and partial differential equation (PDE) model for image denoising. Wavelet coefficients are modeled as waves that grow while expanding along scales. The model establishes a precise link between corresponding modulus maxima in the wavelet domain and then allows predicting wavelet coefficients at each scale from the first one from waves obeying a precise partial differential equation. This as well as characterization of singularities in the wavelet domain required high computational cost, and the method eventually produced visual artifacts.

Bao and Krim [51] addressed the problem of texture losses in diffusion process in scale spaces by incorporating ideas from wavelet analysis. They showed that using wavelet frames of higher order than Haar's is as good as to accounting for longer term correlation structure, while preserving the local focus on equally important features and illustrated the advantages of removing noise while preserving features. The objective measures were not provided and the evaluation was based purely on the visual quality of a few images, so it is hard to judge on the performance of the method.

In [53], Chen developed three denoising schemes by combining PDE with wavelets. In the first proposed model, the diffusion is a function of the Rudin-Osher-Fatemi's total variation model and used amount of advection to diffuse differently in various directions. The performance of the method has proved feasibility of considering local structures for preserving edges in diffusion process. The result shows improvement over Rudin-Osher-Fatemi's total variation model for low level of noise σ = 15, 20, 25 only for Barbara image with an improvement of over 1.5 to 2.0 dB more.

Another approach recently proposed by Nikpour and Hassanpour [57] performs diffusion of approximation coefficients of wavelet transform while applying shrinkage to detail coefficients. The decomposition is a five level wavelet transform using Daubechies10 mother wavelet. The method was compared to median filter, wavelet thresholding, anisotropic diffusion (PM), fourth order PDE. The proposed method improved PSNR on average 0.5-1.5 dB compared to the fourth order PDE, which was found a best among methods under comparison.

Recently, Glenn et al. [59] proposed a highly efficient method for denoising images based on combining the Shearlets with TV. They have obtained estimates from a shearlet representation by constraining the residual coefficients using a projected adaptive total variation scheme.

2.4 Summary

a) The diffusion needs a reliable estimate of image gradients because with an increase in noise level, the effectiveness of the gradient calculation degrades and thus deteriorates the performance of the method.
b) An equal number of iterations in the diffusion of all pixels in the image lead to blurring of textures and fine edges although the smooth regions benefit.
c) There is a need in a better estimate of the local structure for controlling the diffusion especially for medium and high noise levels as the effectiveness of finding the local structure degrades with increasing noise level.
d) Stopping criteria: Based on complete image PSNR fails to smooth some of the local regions.

Models which incorporate the above considerations are discussed further in subsequent chapters: 1) studies of different diffusivity functions in Chapter 3; 2) adaptive diffusion in the image intensity domain in Chapter 4 ; 3) adaptation to the local context in the transform domain in Chapter 5; 4) patch based locally and feature adaptive diffusion in Chapter 6.

CHAPTER 3

IMAGE DIFFUSION IN CONNECTION WITH ROBUST M-ESTIMATORS

In this chapter, we introduce a nonlinear diffusion method for image denoising using robust M-estimators. In the proposed diffusion model, the diffusivity function is replaced by robust M-estimators weight function.

3.1. In search of other diffusivity functions: Robust M-Estimators

Robust statistical methods [62, 63] provide tools for statistics problems in which underlying assumptions are inexact. Applications of robust methods in vision are seen in image restoration, smoothing and clustering/segmentation [64-67], surface and shape fitting [68, 69], registration [70] and pose estimation [71], where outliers are an issue.

There are several types of robust estimators. Among them are the M-estimator (maximum likelihood estimator), L-estimator (linear combinations of order statistics), R-estimator (estimator based on rank transformation) [62], RM estimator (repeated median) [72] and LMS estimator (estimator using the least median of squares) [73]. We are concerned only with the M-estimator weight functions. Table 1 lists some robust functions. They are closely related to the adaptive interaction function. Where $\rho(x)$ is the objective function, $\psi(x)$ is the influence function, $w(x)$ is the weight function and c is the tuning constant**.**

Fig. 3.1 illustrates the bounded diffusivity functions for the above M-estimator weight functions. From the stability graphs it can be observed that robust M-estimators weight functions are nonnegative function similar to that of diffusivity function which controls the amount of diffusion.

Table 3.1 : A commonly used M-estimators

	$\rho(x)$	$\psi(x)$	$w(x)$
L1-L2 [74]	$\left(\sqrt{1+\frac{x^2}{2}}-1\right)$	$\frac{x}{\sqrt{1+\frac{x^2}{2}}}$	$\frac{1}{\sqrt{1+\frac{x^2}{2}}}$
Fair [75]	$c^2[\lvert x\rvert/c-\log(1+\lvert x\rvert/c)]$	$x/(1+\lvert x\rvert/c)$	$1/(1+\lvert x\rvert/c)$
Cauchy [76]	$(c^2/2)\log(1+x^2/c^2)$	$x/(1+x^2/c^2)$	$1/(1+x^2/c^2)$
Geman–McClure [76]	$(x^2/2)/(1+x^2)$	$x/(1+x^2)^2$	$1/(1+x^2)^2$
Welsch [76]	$(c^2/2)[1-\exp(-x^2/c^2)]$	$x\exp(-x^2/c^2)$	$\exp(-x^2/c^2)$

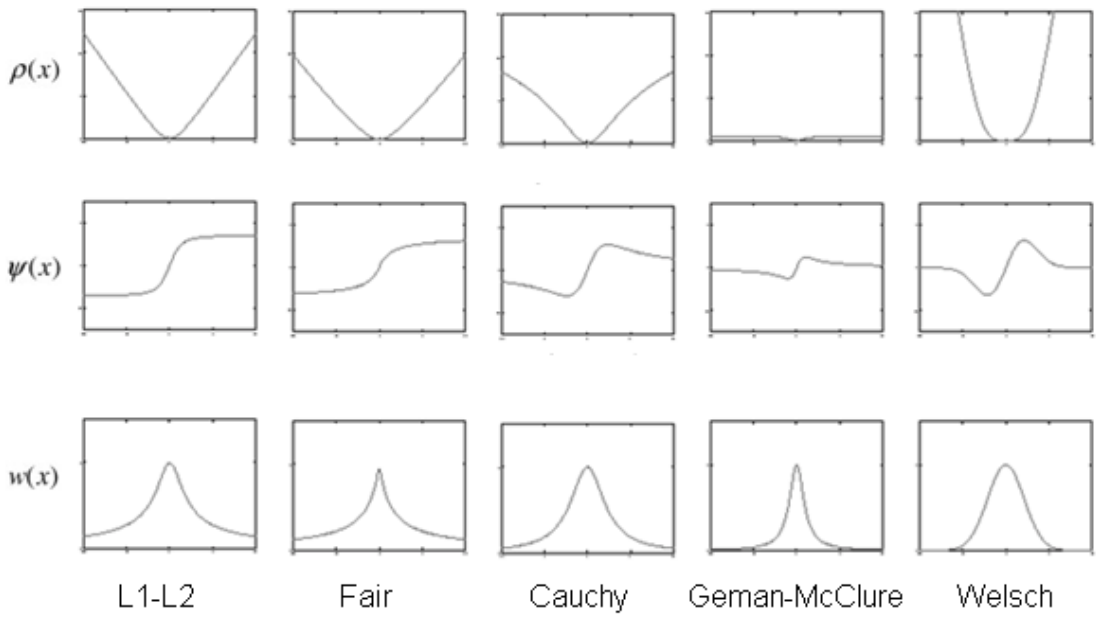

Fig. 3.1 Graphs of Different Robust M-Estimators

3.2 Proof: why m-estimator

Given $\rho : R \to [0,+\infty)$ one can consider the integral functional

$$F(u) := \int \rho(u_x) dx$$

The gradient of F turns out to be

$$\nabla F(u) = -(\psi(u_x))_x = -w(u_x)u_{xx}$$

The gradient flow of F is formally the equation

$$u' = -\nabla F(u)$$

which becomes the PDE

$$u_t = (\psi(u_x))_x = w(u_x)u_{xx}$$

The following facts are equivalent

a) ρ - function is convex in a given range.

b) ψ is increasing in the same range.

c) w-weight function is monotonically decreasing function i.e., the gradient flow of the weight function is a forward parabolic PDE in the given range.

Therefore, the above mentioned equations are an example of gradient flow of non convex functional.

3.3 Experimental results

The algorithm is tested on a number of benchmark images degraded by AWG noise of μ=0 and σ = 10, 20, 30, 50, and 100. For comparison we select PM [13] and the results obtained for different robust weight functions. Table 3.2 shows PSNR values by the

different robust weight functions for benchmark images and Table 3.3 shows UIQI values by the different robust weight functions for benchmark images. From the results it clearly shows that robust weight functions performs much better compare to PM model.

Table 3.2. PSNR results of different robust weight functions.

Method	**Image**	**10**	**20**	**30**	**50**	**100**
PM	Lena	33.78	29.85	25.52	18.24	9.49
	Peppers	33.76	30.20	25.74	18.26	9.46
	Cameraman	34.48	29.48	24.85	17.98	9.44
	House	37.11	32.16	26.59	18.52	9.49
Cauchy	Lena	33.99	30.52	28.47	25.71	21.75
	Peppers	34.01	30.94	30.28	25.89	21.32
	Cameraman	34.84	30.41	27.28	24.56	20.43
	House	37.04	33.01	30.64	27.53	22.85
Fair	Lena	34.06	30.98	29.28	27.25	24.75
	Peppers	33.94	31.13	29.46	27.32	24.48
	Cameraman	34.83	30.97	28.84	26.28	23.05
	House	**37.84**	**34.29**	32.27	29.79	26.56
L1-L2	Lena	**34.19**	**31.11**	**29.45**	**27.48**	**25.05**
	Peppers	**34.18**	**31.45**	**29.82**	**27.72**	**24.85**
	Cameraman	**35.11**	**31.24**	**29.12**	**26.61**	**23.46**
	House	37.52	34.23	**32.42**	**30.20**	**27.18**
Welsch	Lena	33.41	30.65	28.46	22.53	11.72
	Peppers	33.64	30.94	28.85	22.57	11.55
	Cameraman	34.21	30.40	27.57	21.59	11.45
	House	36.99	33.73	31.02	23.38	11.80

Table 3.3. UIQI results of different robust weight functions.

Method	**Image**	**10**	**20**	**30**	**50**	**100**
PM	Lena	0.6684	0.5388	0.3699	0.1428	0.0556
	Peppers	0.6518	0.5502	0.4020	0.1671	0.0621
	Cameraman	0.6287	0.4886	0.3426	0.1598	0.0932
	House	0.5566	0.4080	0.2426	0.0919	0.0399
Cauchy	Lena	0.6689	0.5521	0.4673	0.3430	0.1794
	Peppers	0.6527	0.5610	0.4967	0.3931	0.2359
	Cameraman	0.6368	0.4998	0.4114	0.2945	0.1533
	House	0.5360	0.3962	0.3022	0.2010	0.0960
Fair	Lena	0.6753	0.5667	0.5001	0.4173	0.3133
	Peppers	**0.6599**	0.5702	0.5177	0.4497	0.3620
	Cameraman	0.6355	0.5111	0.4440	**0.3655**	**0.2651**
	House	**0.5510**	**0.4531**	**0.3860**	**0.3078**	**0.2195**
L1-L2	Lena	**0.6776**	**0.5693**	**0.5031**	**0.4189**	**0.3123**
	Peppers	0.6582	**0.5703**	**0.5207**	**0.4561**	**0.3648**
	Cameraman	**0.6372**	**0.5156**	**0.4470**	0.3640	0.2607
	House	0.5265	0.4079	0.3430	0.2744	0.2007
Welsch	Lena	0.6356	0.5555	0.4799	0.2797	0.0459
	Peppers	0.6081	0.5614	0.5048	0.3253	0.0595
	Cameraman	0.6035	0.5027	0.4279	0.2656	0.0748
	House	0.5392	0.4560	0.3700	0.1873	0.0262

Fig. 3.2 First row: “Lena” image and that with AWG noise, σ =30;

Second row: Results by Cauchy and Fair; Third row: Results by L1-L2 and Welsch.

Fig. 3.3 First row: “Lena” image and that with AWG noise, σ =100;

Second row: Results by Cauchy and Fair; Third row: Results by L1-L2 and Welsch.

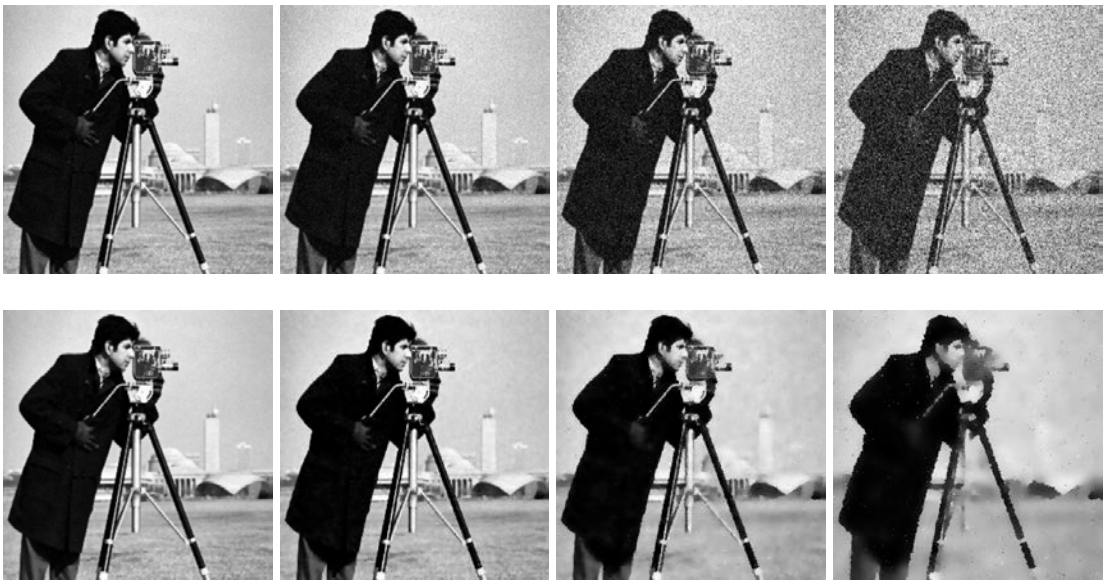

Fig.3.4 First row: “Cameraman” image and that with AWG noise, σ =10, 20, 50 and 100; Second row: Corresponding results of Cauchy.

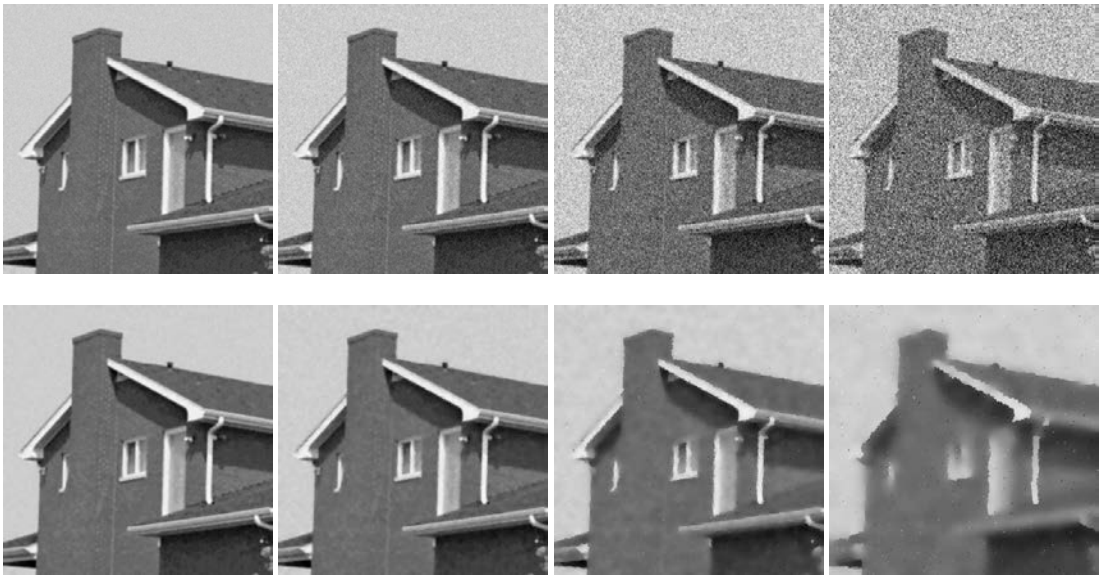

Fig.3.5 First row: “House” image and that with AWG noise, σ =10, 20, 50 and 100; Second row: Corresponding results of Cauchy.

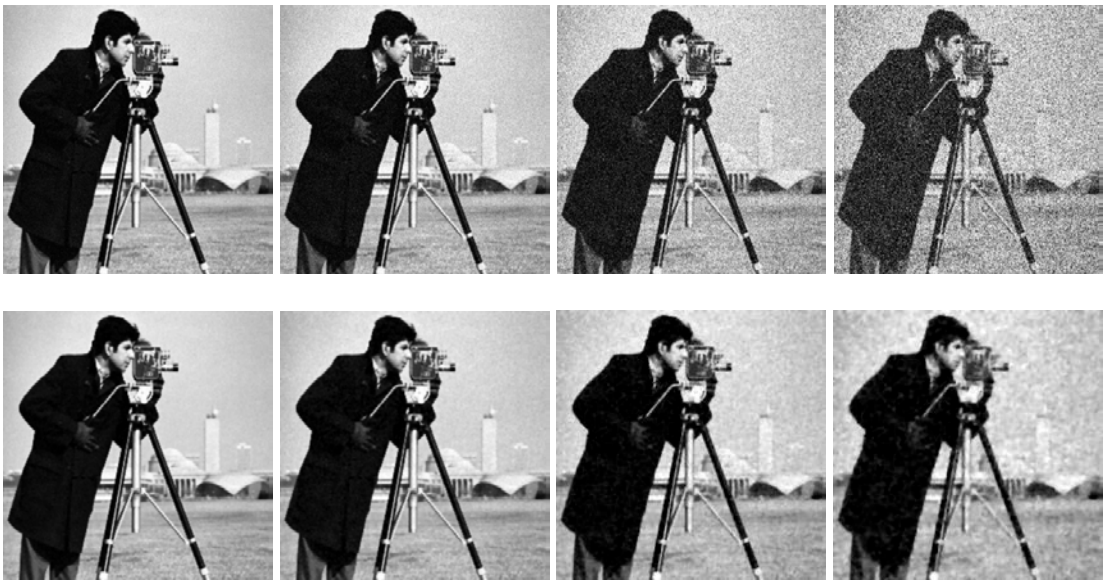

Fig.3.6 First row: “Cameraman” image and that with AWG noise, σ =10, 20, 50 and 100; Second row: Corresponding results of Fair.

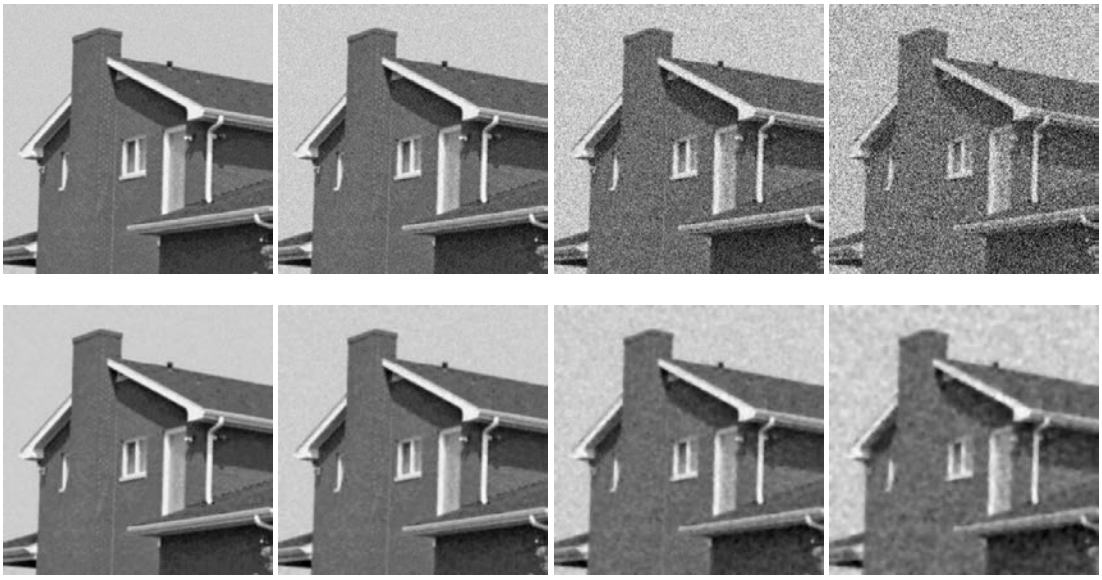

Fig.3.7 First row: “House” image and that with AWG noise, σ =10, 20, 50 and 100; Second row: Corresponding results of Fair.

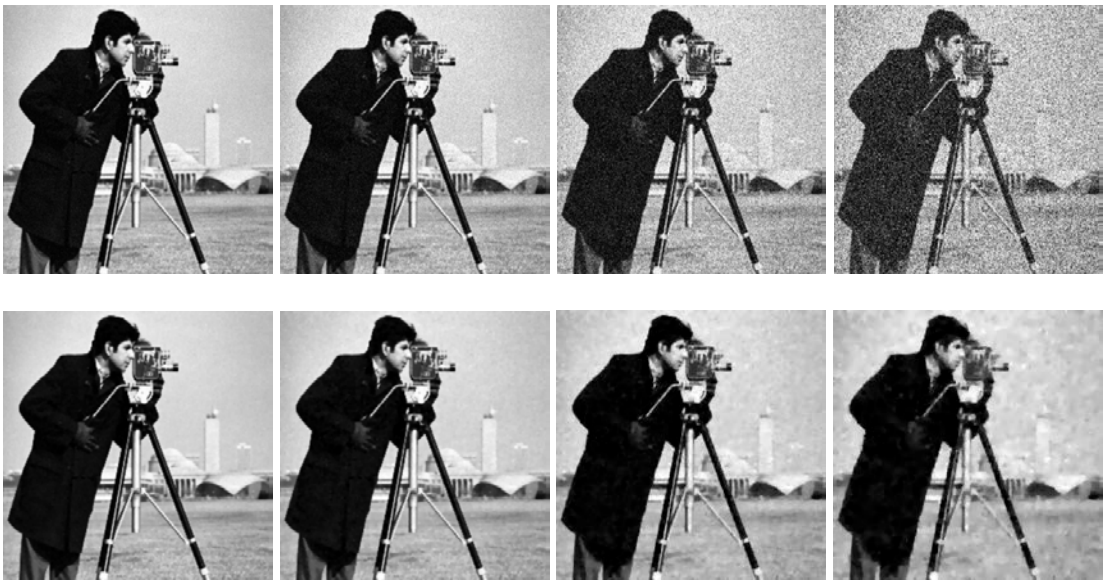

Fig.3.8 First row: “Cameraman” image and that with AWG noise, σ =10, 20, 50 and 100; Second row: Corresponding results of L1-L2.

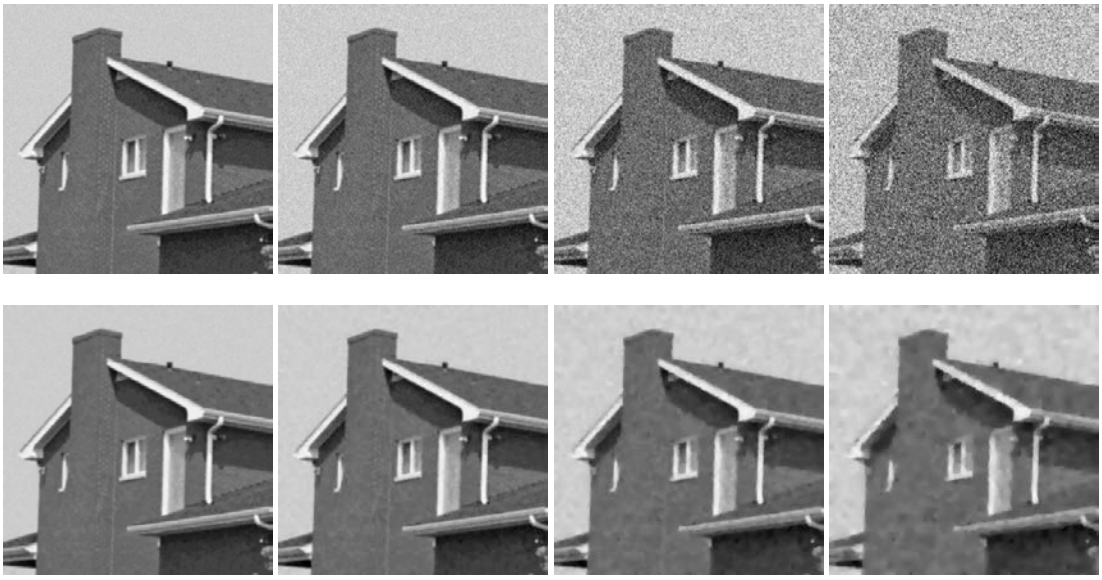

Fig.3.9 First row: “House” image and that with AWG noise, σ =10, 20, 50 and 100; Second row: Corresponding results of L1-L2.

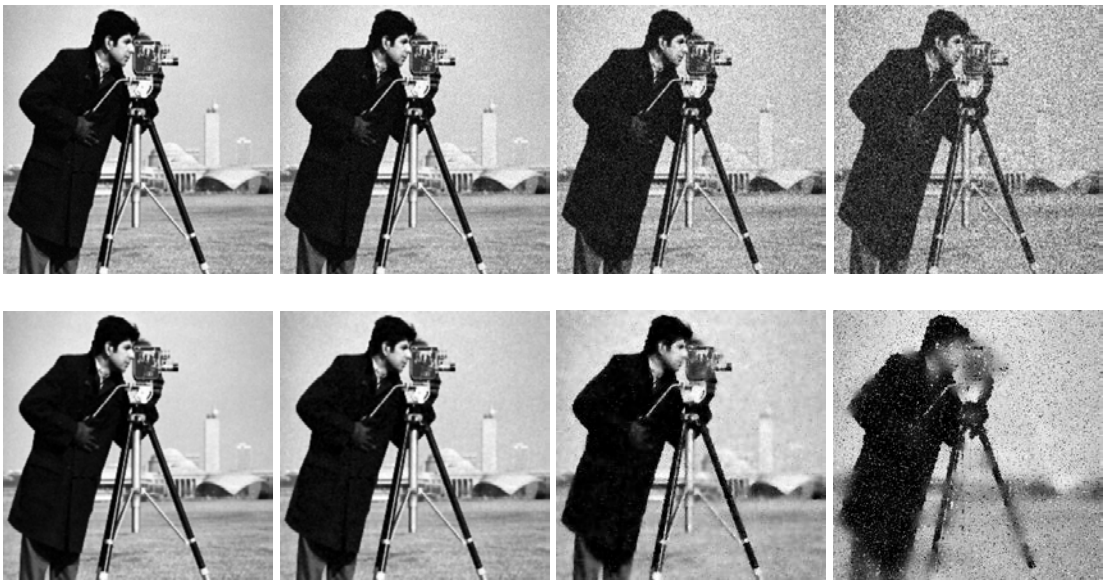

Fig.3.10 First row: “Cameraman” image and that with AWG noise, σ =10, 20, 50 and 100; Second row: Corresponding results of Welsch.

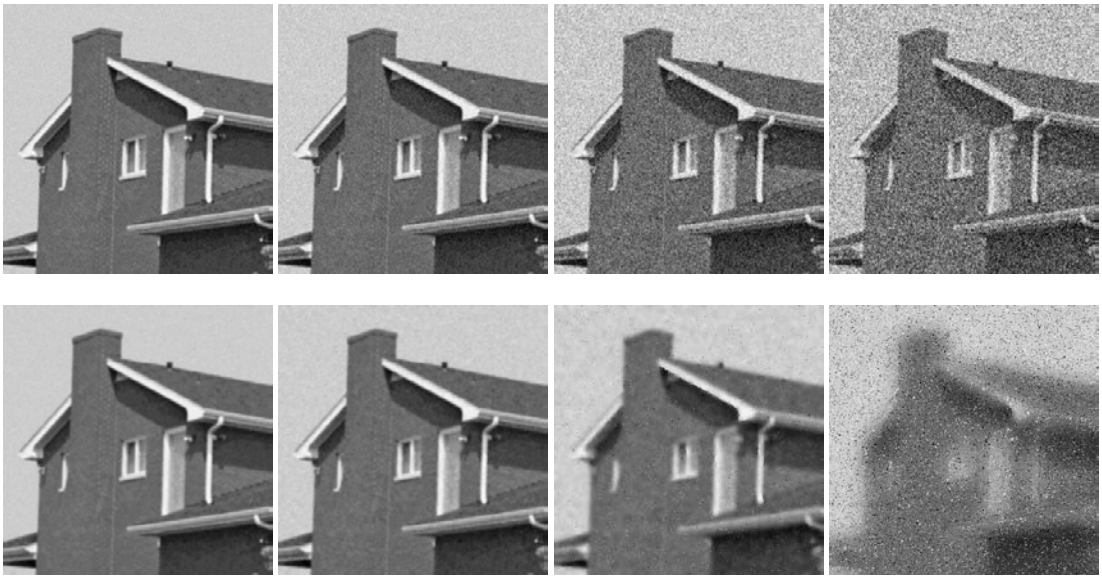

Fig.3.11 First row: “House” image and that with AWG noise, σ =10, 20, 50 and 100; Second row: Corresponding results of Welsch.

In Fig.3.2 we show “Lena” image and results of diffusion using different robust weight functions with λ =10 for additive Gaussian noise with standard deviation σ = 30. In

Fig.3.3 we show “Lena” image and results of diffusion using different robust weight functions with λ =10 for additive Gaussian noise with standard deviation σ = 100. The denoising performance of the different robust weight functions is further illustrated in Fig. 3.4- 3.11, where we show noisy (i.e., σ=10, 20, 50, and 100) test images and corresponding denoised images. From the results it can be observed that new method using Fair’s and L1-L2 weight functions performs better in terms of both subjective quality and objective measures compared to PM diffusivity.

3.4 Conclusion

In this Chapter, we have introduced a nonlinear diffusion method for image denoising using robust M-estimators. In the proposed diffusion model, the diffusivity function is replaced by robust M-estimators weight function. The robust M-estimators outperforms the Perona-Mallik diffusion both in terms of objective and subjective quality.

CHAPTER 4

LOCAL BINARY PATTERN BASED DIFFUSION

In this chapter we present a novel local binary pattern (LBP) based adaptive diffusion for additive white gaussian noise reduction. The LBP operator unifies traditionally divergent statistical and structural models of region analysis. We use LBP textons to classify an image around a pixel into noisy, homogenous, corner and edge regions. According to different types of regions, a variable weight is assigned in to the diffusion equation, so that our algorithm can adaptively encourage strong diffusion in homogenous/ noisy regions and less on the edge/ corner regions.

4.1 Local binary pattern

Ojala et al. [77] first introduced the LBP operator for texture classification. Success in terms of speed, accuracy and performance is reported in many active research areas such as texture classification [78-81], object detection [82-84], face recognition [85-89] and image retrieval[90, 91]. The LBP operator combines characteristics of statistical and structural texture analysis: it describes the texture with primitives called as textons.

Fig.4.1 shows how a texton and LBP code are derived; the LBP takes the 3x3 neighborhood of a central pixel and generates a binary 1 if the neighbor of that pixel has a larger value than the otherwise, it produces a binary 0. An LBP code for a neighborhood is produced by multiplying the threshold values with weights given to the corresponding pixels, and summing up the result. Thus each LBP can be regarded as a micro-texton [77].

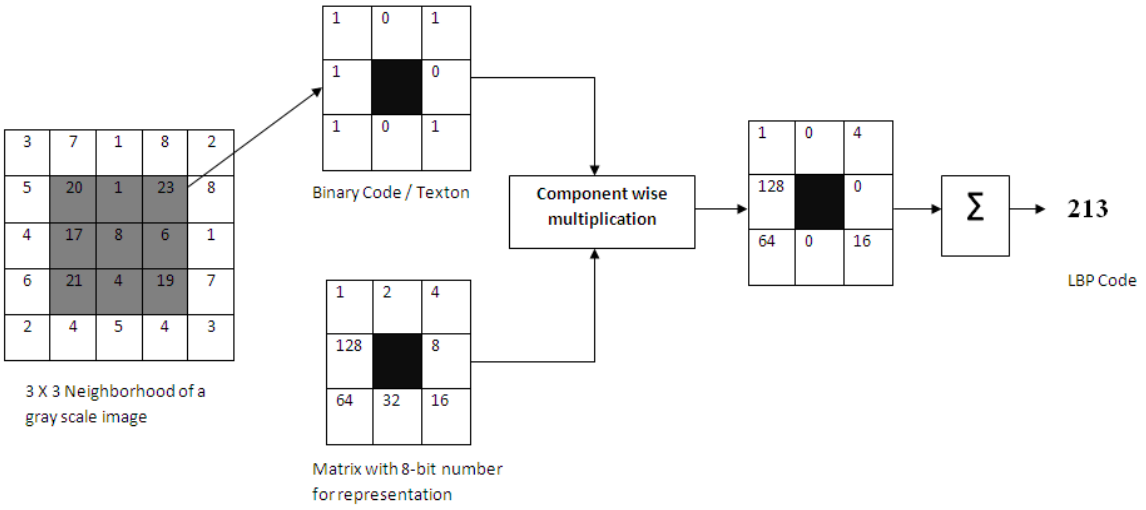

Fig.4.1. Example of obtaining LBP for 3x3 neighborhood

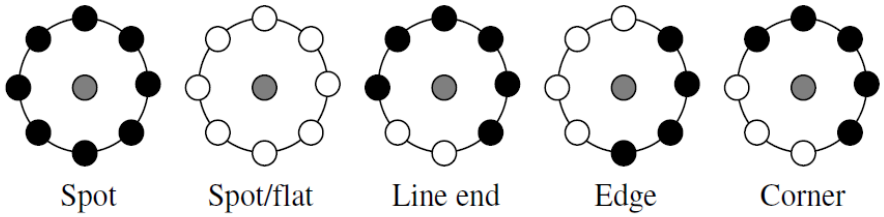

Fig.4.2. Different texture primitives detected by the LBP [77]

Local textons include spots, flat areas, edges, line ends and corners. Fig.4.2 shows the different texture primitives detected by the LBP. In the figure, gray circle indicates center pixel, white circles indicate ones and zeros are indicated by black.

4.2 Local binary pattern based diffusion (LBPD)

In this section, we summarize the idea of the local binary pattern based diffusion scheme. For each pixel (i,j) of the image we use a 3x3 neighborhood window. For each neighbor

with respect to (i,j) corresponds to one direction {N= North, S= South, W = West, E= East}. If we denote I as the input image and *x* is the 3x3 neighborhood window, then the gradient $\nabla_p x(i, j) = x(i+m, j+n) - x(i, j)$ with (m, n)Є {-1,0,1} where (m,n) corresponds to one of the four directions and (i,j) is called the center of the gradient. We derive the LBP texton for the same 3x3 window as shown in Fig.1. This textons can be used to determine whether the center pixel is spot/flat/edge/line/corner pixel. According to different types of pixel contexts the discrete diffusion is performed based on Eq. 4 with the diffusivity function c_1, relative adjustments to weights of the diffusion are made such strong diffusion on spot/ flat pixels i.e. ∇t = 0.04 is encouraged whereas edge/line/corner pixels are diffused slower/lesser i.e. ∇t = 0.01.The following steps are performed until the PSNR decreases in the subsequent iteration.

4.2.1 LBPD Algorithm

1. Input the image data I.
2. Place the window W at (i,j), store the image I values inside W in x
3. Derive the LBP texton as shown in Fig. 1.,if LBP texton is spot or flat then ∇t = 0.04 else ∇t = 0.01
4. Calculate the local gradient using equation

   $\nabla_N x_{i,j} = x_{i-1,j} - x_{i,j}$; $\nabla_S x_{i,j} = x_{i+1,j} - x_{i,j}$ $\nabla_E x_{i,j} = x_{i,j+1} - x_{i,j}$; $\nabla_W x_{i,j} = x_{i,j-1} - x_{i,j}$
5. Use the discrete diffusion equation to diffuse

   $$I_{i,j}^{n+1} = I_{i,j}^{n} + (\nabla t) \bullet \begin{bmatrix} c_N(\nabla_N x_{i,j}^n) \bullet \nabla_N x_{i,j}^n + c_S(\nabla_S x_{i,j}^n) \bullet \nabla_S x_{i,j}^n + \\ c_E(\nabla_E x_{i,j}^n) \bullet \nabla_E x_{i,j}^n + c_W(\nabla_W x_{i,j}^n) \bullet \nabla_W x_{i,j}^n \end{bmatrix}$$

   let output $I(i,j) = I_{i,j}^{n+1}$
6. Repeat 3 to 5 until the PSNR decreases in the subsequent iteration

4.3 Experiment results

Table 4.1 and 4.2 shows the PSNR and UIQI attained by LBPD with the additive Gaussian noise of μ=0 and σ = 10, 20, 30, 50, and 100. Fig. 4.3 allows for evaluating the visual quality of the resultant images produced by LBPD. We observe that the proposed method works better in for low noise levels but fails at high noise levels because of its inability to recognize the textons at high noise levels. Specifically, they are diffused in a greater extent while preserving edges and local details.

Fig. 4.3. First row: "Lena" image and that with AWG noise, σ =10 and 100; Second row: Corresponding results by LBPD.

Table 4.1. PSNR results of PM and the proposed LBPD Method.

Method	**Image**	**10**	**20**	**30**	**50**	**100**
PM	Lena	33.78	29.85	25.52	18.24	9.49
	Peppers	33.76	30.20	25.74	18.26	9.46
	Cameraman	34.48	29.48	24.85	17.98	9.44
	House	37.11	32.16	26.59	18.52	9.49
LBPD	Lena	**34.27**	**31.17**	**28.50**	**27.06**	**24.94**
	Peppers	**34.24**	**31.48**	**28.84**	**27.19**	**24.70**
	Cameraman	**35.16**	**31.29**	**27.60**	**25.88**	**23.22**
	House	**37.59**	**34.28**	**31.73**	**29.83**	**27.02**

Table 4.2. UIQI results of PM and the proposed LBPD Method.

Method	**Image**	**10**	**20**	**30**	**50**	**100**
PM	Lena	0.6684	0.5388	0.3699	0.1428	0.0556
	Peppers	0.6518	0.5502	0.4020	0.1671	0.0621
	Cameraman	0.6287	0.4886	0.3426	0.1598	0.0932
	House	0.5566	0.4080	0.2426	0.0919	0.0399
LBPD	Lena	**0.6781**	**0.5702**	**0.4712**	**0.4042**	**0.3100**
	Peppers	**0.6587**	**0.5709**	**0.5004**	**0.4487**	**0.3659**
	Cameraman	**0.6379**	**0.5163**	**0.4185**	**0.3469**	**0.2516**
	House	**0.5272**	**0.4084**	**0.3033**	**0.2546**	**0.1933**

4.4 Conclusion

We have described a novel feature-preserving adaptive non-linear diffusion algorithm based on local binary pattern texton. The proposed method is based on local structure and

involves local binary texton for the denoising process. First, we classify the centre pixel as edge, spot, flat region, line end or corner using LBP texton. According to different types of pixel texton, relative adjustments to weights of the diffusion are made such strong diffusion on spot/flat pixels is encouraged whereas edge/line/corner pixels are diffused slower/lesser. We believe this method represents an important step forward for the use of neighborhood design that captures local context in images. Experimental results demonstrate its potential for the feasibility of structure context based controlled diffusion approach for low noise levels.

CHAPTER 5

SWCD: STATIONARY WAVELET DOMAIN CONTEXT BASED DIFFUSION

In this chapter, we propose a context adaptive nonlinear diffusion method for image denoising in wavelet domain which we called SWCD. In diffusing detail coefficients, the method adapts to the local context such that strong edges are preserved and smooth regions are diffused in a greater extent. The local context which is derived directly from the transform energies at scales 1 and 2 of two-level stationary wavelet transform (SWT) [92] controls the diffusion. The shift invariance of SWT contributes to the performance of the method.

5.1 Stationary wavelet domain context based diffusion (SWCD)

In a decimated discrete wavelet transform (DWT) after high and low pass filtering, coefficients are down sampled. Although this prevents redundancy and allows for using a same pair of filters in different scales, this decimated transform lacks shift invariance. Thus, small shifts in the input signal can cause major variations in the distribution of energy of coefficients at different scales. Even with periodic signal extension, the DWT of a translated version of a signal is not, in general, the translated version of the DWT of X. To restore the translation invariance one can average a slightly different DWT, called ε-decimated DWT, to define SWT [92]. SWT can be obtained by convolving the signal with the appropriate filters as in the DWT case but without down-sampling. The two-dimensional SWT leads to a decomposition of approximation coefficients at scale j to four components: the approximation at scale $j+1$, and the details in three orientations,

i.e., horizontal, vertical, and diagonal). Considering the multi-sampling filter banks, SWT decomposition is as below:

$$A_{j,k_1,k_2} = \sum_{n_1}\sum_{n_2} h_0^{\uparrow 2^j}(n_1 - 2k_1)h_0^{\uparrow 2^j}(n_2 - 2k_2)\, A_{j-1,n_1,n_2}$$

$$D^1_{j,k_1,k_2} = \sum_{n_1}\sum_{n_2} h_0^{\uparrow 2^j}(n_1 - 2k_1)h_1^{\uparrow 2^j}(n_2 - 2k_2)\, A_{j-1,n_1,n_2}$$

$$D^2_{j,k_1,k_2} = \sum_{n_1}\sum_{n_2} h_1^{\uparrow 2^j}(n_1 - 2k_1)h_0^{\uparrow 2^j}(n_2 - 2k_2)A_{j-1,n_1,n_2}$$

$$D^3_{j,k_1,k_2} = \sum_{n_1}\sum_{n_2} h_1^{\uparrow 2^j}(n_1 - 2k_1)h_1^{\uparrow 2^j}(n_2 - 2k_2)\, A_{j-1,n_1,n_2} \qquad (3),$$

Where $h_0^{\uparrow 2^j}, h_1^{\uparrow 2^j}$ denote the (2^j-1) zero padding. The inverse transform of SWT follows Eq.4.

$$\begin{aligned} A_{j-1,n_1,n_2} = \frac{1}{4}\sum_{i=0}^{3}\{ & \sum_{k_1}\sum_{k_2} l_0(n_1 - 2k_1 - i)\, l_0(n_2 - 2k_2 - i)A_{j,k_1,k_2} \\ & + \sum_{k_1}\sum_{k_2} l_0(n_1 - 2k_1 - i)\, l_1(n_2 - 2k_2 - i)D^1_{j,k_1,k_2} \\ & + \sum_{k_1}\sum_{k_2} l_1(n_1 - 2k_1 - i)\, l_0(n_2 - 2k_2 - i)D^2_{j,k_1,k_2} \\ & + \sum_{k_1}\sum_{k_2} l_1(n_1 - 2k_1 - i)\, l_1(n_2 - 2k_2 - i)D^3_{j,k_1,k_2}\} \end{aligned} \qquad (4),$$

where *A* and *D* are approximation and detail coefficients, respectively; l_0 and l_1 are low-pass and high-pass filters, respectively

From (3) and (4), we can verify that SWT includes redundant information and has the shift-invariance suitable for structure analyses and denoising. Smooth regions in image are represented mainly by approximation coefficients. According to the way transform is performed, energies of strong edges are doubled and the noise and fine textures vanish from low to high transform scales. Thus, distribution of the transform energies carries important information about the local context. Consider two-levels of

SWT of the image with the Haar wavelet. Assuming zero-mean for details coefficients, the energy of the transform in respective subbands is defined as follows:

$$E_{s,k} = \sum_{i=1}^{n} \sum_{j=1}^{m} | D_{i,j,k} |^2 \qquad (5),$$

where nxm is a window at scale s={1,2}, and k={v,d,h}, v- vertical, d –diagonal and h-horizontal subband.

The ratio of transform energies in different subbands, R_k is calculated as follows:

$$R_k = \frac{E_{2,nxm,k}}{E_{1,nxm,k} + \varepsilon} \qquad (6),$$

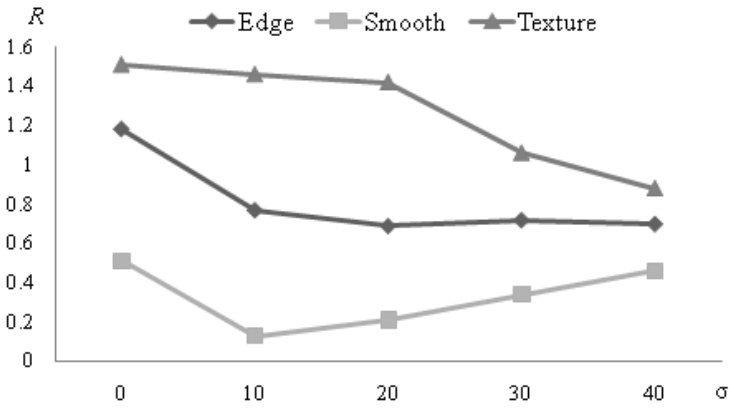

Fig.5.1 Distribution of E_2/E_1 for different contexts vs Gaussian white noise σ= 10,20,30,40

where ε = 0.001. The energy is calculated in 3x3 sliding window per pixel so that up-sampled image of the second level of transform would incorporate the filtered edge information from the first level of Haar transform. An example in Fig.5.1 shows representatives of R_k derived from sample image regions for originals and their noisy

variants with Gaussian noise of σ= 10, 20, 30, 40. For simplification, the energies in the figure are cumulative energies in all three details subbands. This ratio characterizes the local context for controlling the diffusion equation.

Eq. (7) below defines general case WF diffusivity equation.

$$g(\Delta x) = 1 - \exp\frac{-C_m}{\left[\left|\Delta x\right| / \lambda\right]^{2m}} \qquad (7),$$

where $|\Delta x|$ is the gradient estimate; λ is the conductance or diffusivity constant and constant C_m = 2.33666, 2.9183 and 3.31488 for m = 2, 3 and 4, respectively. It was also shown by Weickert that the best results are attained with m=2.

As it was shown in [36], solving the PDE by means of finite differences with Haar wavelet leads to the modification of WF diffusivity, s_θ is given by

$$s_\theta(x) = x(1 - 4\mathcal{T} g(|\sqrt{2}x|)) \qquad (8)$$

where $\mathcal{T}$ is the time step size and has to fulfill condition $\mathcal{T} \leq 0.25$.

Substitution of Eq. 7 in Eq.8 with time step size $\mathcal{T} = 0.25$, leads to a modified diffusivity function

$$s_\lambda(x) = x \cdot exp\left(\frac{-c_m}{(\sqrt{2}\cdot|x|/\lambda)^{2m}}\right) \qquad (9)$$

5.1.1 SWCD Algorithm:

In the proposed method the edge estimate is given by $|x(p,q)| = \left|D_1^{(k)}(p,q)\right|$ and detail coefficients in a smooth region, that is those with the context R_k< 0.5 undergo

additional two diffusion steps. That provides more diffusion allowance for smooth regions. The method performs according to the following steps:

1. *Image is decomposed to two levels by means of SWT with Haar wavelet.*
2. *The context, i.e. R_k per each coefficient of detail subbands is calculated according to (6).*
3. *Run 1: Detail coefficients are diffused* as

   $$D_1^{(k+1)} = D_1^{(k)} * exp\left(\frac{-2.9183}{\left(\sqrt{2}\left|D_1^{(k)}(p,q)\right|/\lambda\right)^4}\right)$$

   where $D_1^{(0)} = x(p,q)$ *for p,q=1,2…n of nxnimage.*
4. *If R_k<0.5, Step 3 is repeated twice (Run 2 and 3), otherwise Step 5 is performed.*
5. *The image is synthesized by applying the inverse SWT.*
6. *Steps 1-5 are repeated (iterated) until the best solution is obtained, that is, the PSNR decreases in the subsequent iteration.*

5.2 Parameter Selection

Fig. 5.2 shows PSNR of the SWCD results for a fixed noise level (σ= 40) with different values of λ= 10, 50,100 and 150 and iterations for "Lena" image. The plot provides the indication of that λ= 100 is a best choice.

Fig.5.3 shows PSNR plots for noise levels as σ= 10, 20, 30 and 40 with a fixed value of λ= 100 and different number of iterations for "Lena" image indicating the number of iterations towards the best PSNR as 10.

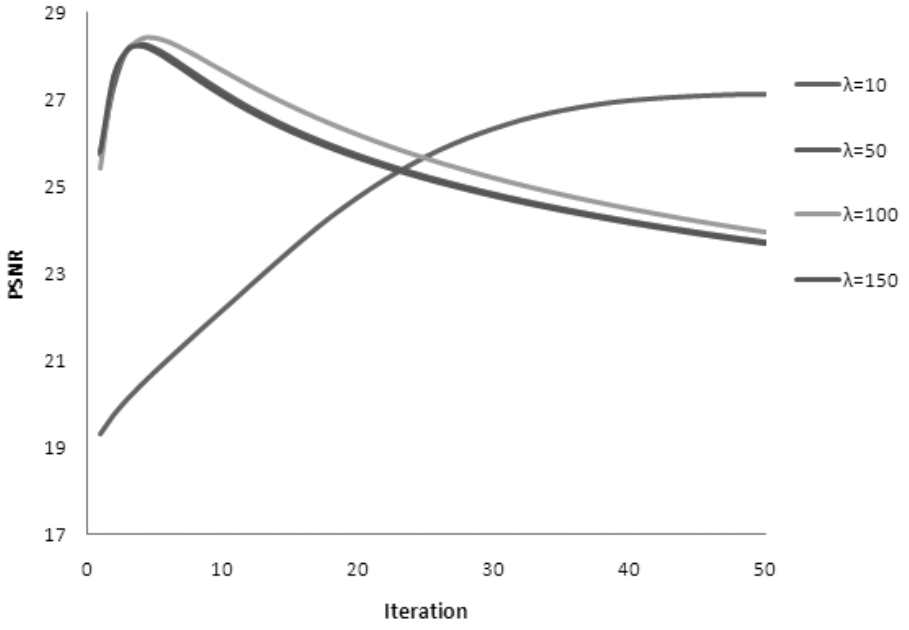

Fig.5.2 PSNR obtained using λ=10, 50,100 and 150 with a noise level σ= 40 for "Lena"

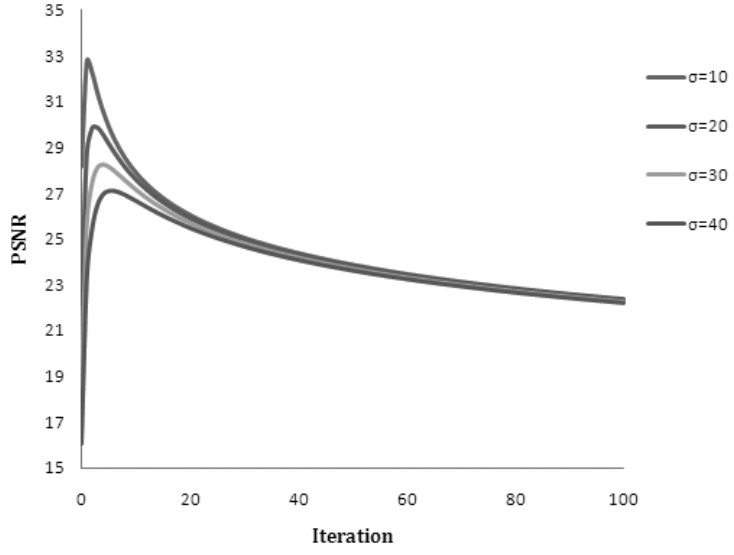

Fig.5.3 PSNR values obtained for different noise values (σ = 10, 20, 30 and 40) in the diffusivity function with λ= 100 for "Lena" image

5.4 Experimental results

Fig.5.4 shows mapping of contexts for “Lena” image for noise levels σ = 10, 20, 30 and 40 based on R_k. Here, darker pixels are used for context $R_k>0.5$. Fig.5.5 shows the SWCD diffusion run maps for “Lena” image for noise level σ = 20. It indicates how R_k changes the number of runs in the implementation of diffusion for the image. Fig.5.6 displays the overall iteration maps for “Lena” image for σ = 10, 20, 30 and 40. Here, darker pixels are for lesser diffused coefficients. The color bar indicates how many times the pixel is undergone the diffusion.

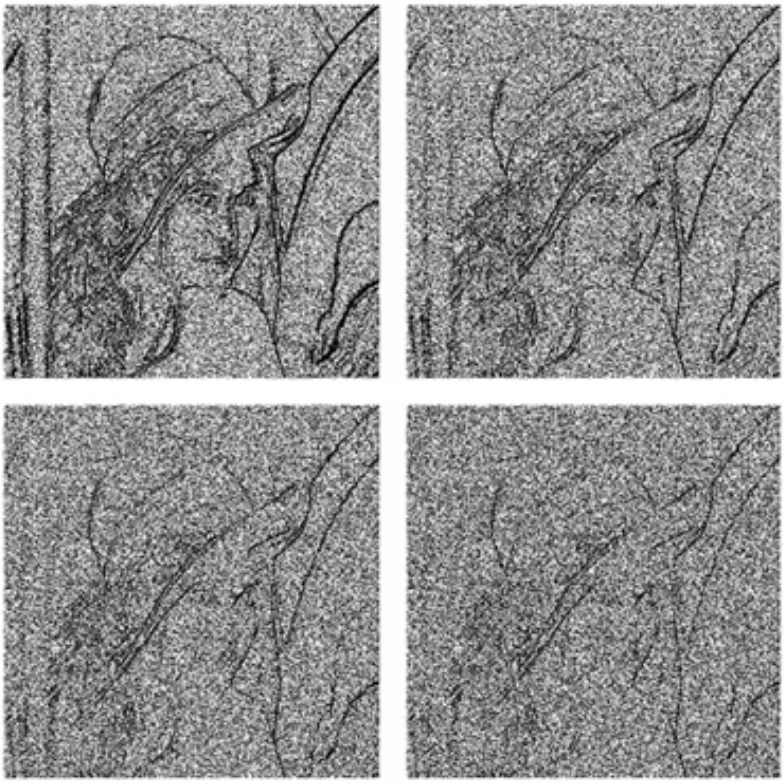

Fig.5.4 Context maps of “Lena”: First row: for noise levels σ = 10, 20; Second row: for noise levels σ = 30 and 40.

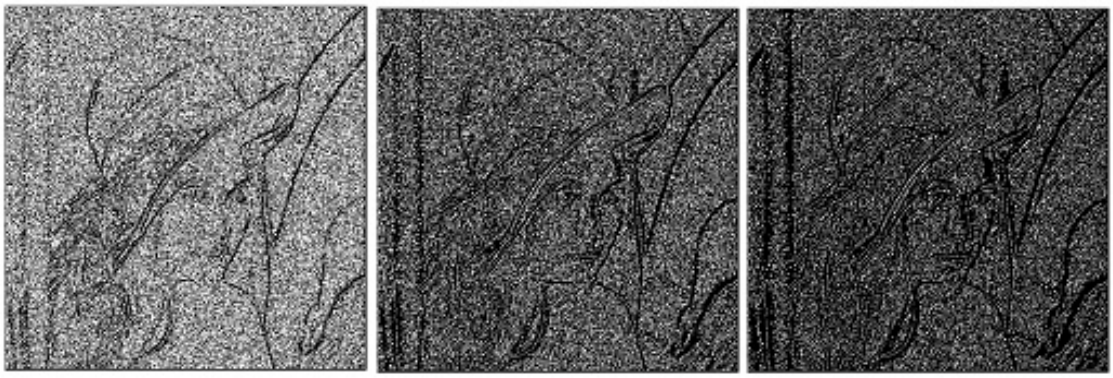

Fig.5.5 Run maps: Initial map of "Lena" with noise σ = 20; second and third runs.

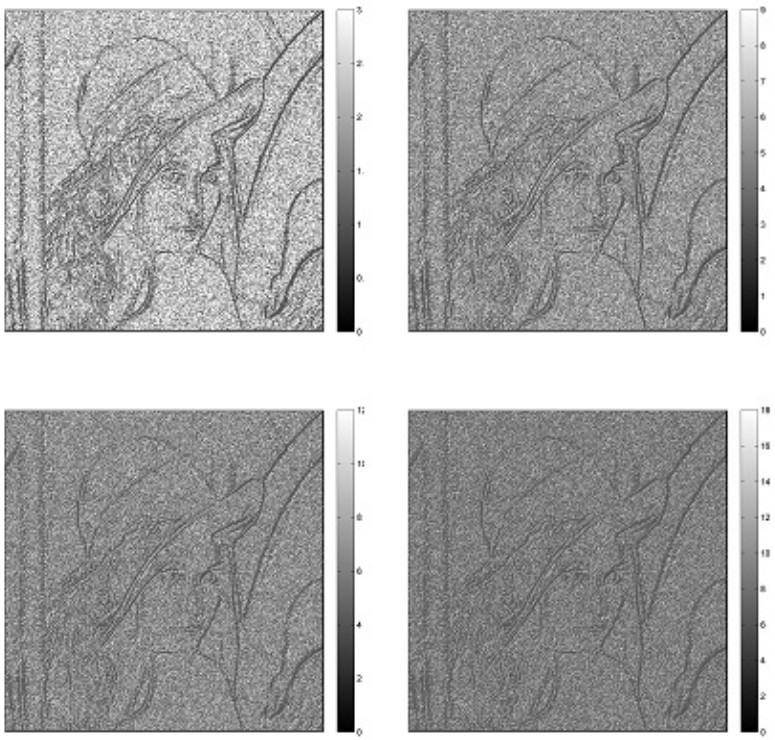

Fig.5.6 Diffusion iteration maps of "Lena". First row: for noise levels σ = 10, 20; second row for noise with σ = 30 and 40.

Table 5.1 PSNR results of the proposed SWCD method

Image/σ	σ= 10	σ= 20	σ= 30	σ= 40
Cameraman	33.57	30.11	28.13	26.76
Lena	32.70	29.79	28.17	26.99
House	35.35	33.05	30.90	29.35
Peppers	32.45	29.85	28.30	27.24

Table 5.2 UIQI results of the proposed SWCD method

Image/σ	σ= 10	σ= 20	σ= 30	σ= 40
Cameraman	0.5278	0.4237	0.3680	0.3284
Lena	0.6479	0.5342	0.4803	0.4336
House	0.5236	0.4620	0.3948	0.3512
Peppers	0.6408	0.5507	0.4915	0.4590

Table 5.3. Comparison (PSNR) of Shih's and SWCD methods

Image/σ	With Noise (dB)	WD	SWCD
House	26.76	32.04	34.91
Cameraman	24.32	31.37	32.76
Peppers	29	32.34	33.23

Table 5.1 and 5.2 presents PSNR and UIQI results attained by SWCD for several benchmark images with the noise levels of σ = 10, 20, 30 and 40. Tables 5.3 present comparison of PSNR reported for the reference method at level of noise reported in respective publication.

Fig.5.7 First row: “Lena” image with noise level σ = 10 and 40;
Second row: Corresponding SWCD results

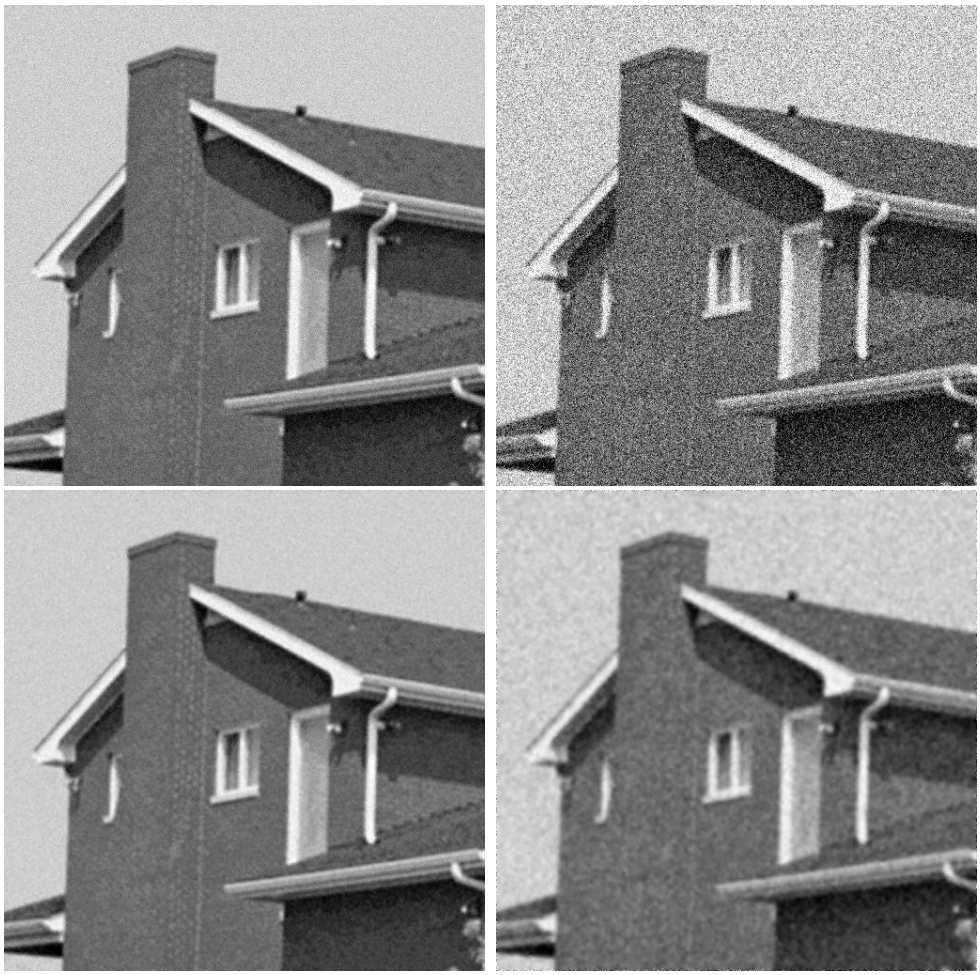

Fig.5.8 First row: “House” image with noise level σ = 10 and 40;

Second row: Corresponding SWCD results

Figures 5.7 and 5.8 are presented for evaluating the visual quality the resultant images produced by SWCD. In texture images and edges created by extended objects as it can be observed diffusion does not cause a significant blur or visual artifacts.

5.5 Conclusion

This chapter has presented an adaptive non-linear wavelet diffusion method. Detail coefficients are diffused selectively depends on the energy distribution across the scales

in two-level SWT. Shift invariance of SWT allows for deriving context information in details subbands and thus has contributed to the performance of the method. Unlike other context-based denoising models, here neither segmentation nor edge detection is performed. The method has been compared to a fairly large number of recently developed denoising techniques which explore the adaptation concept for shrinkage or diffusion. Based on the evaluation results, it can be concluded that the textures and edges are preserved by SWCD and no visual artifacts are created. The proposed method outperforms Shih's method under comparison and that is specifically noticeable for medium noise level. The implementation is computationally efficient as it does not demand on classification or edge detection.

CHAPTER 6

LFAD: LOCALLY- AND FEATURE-ADAPTIVE DIFFUSION

State-of-the art denoising techniques all rely on patches, whether for dictionary learning [27, 28], collaborative denoising of blocks of similar patches [30], or non-local sparse models [93]. Regularization with non-local patch-based weights has shown improvements over classical regularization involving only local neighborhoods [94, 95, 96]. The shape and size of patches should adapt to anisotropic behavior of natural images [97, 98]. In spite of the high performance of patch-based denoising methods, they generally produce artifacts even at comparatively moderate noise levels.

a) KLLD [2] denoising for $\sigma = 25$ b) BM3D [3] denoising for $\sigma = 60$

Fig. 6.1 Results of two patch-based denoising methods: a) KLLD and b) BM3D.

Examples of such visual artifacts are presented in Fig. 6.1 for two state-of-the-art methods, i.e., KLLD [28] and BM3D [30]. The size of the patch has a significant impact on the PSNR value even for similar or identical contents. Fig .4 shows that equal-size

regions of the same structural content from different parts of the image could be diffused differently. Thus, both the structural content and the location of the patch are to be taken into account. Unlike block-transform based methods such as BM3D, which perform with a pre-determined optimum block size, and clustering-based denoising methods, such as KLLD, which use a predetermined optimum number of classes, our method searches for an optimum patch size through iterative diffusion starting with a small patch size, and proceeds with aggregating patches until a best PSNR is attained. We use superpixel segmentation [99] because it produces an over-segmented image of almost equally-sized patches, and thus is the best choice for initializing the method. We explain the selection of the initial number of patches, or, alternatively, the initial size of the patch for different noise levels. To determine the amount of diffusion, we use the inverse difference moment (IDM) feature [33]. We demonstrate that the feature is robust in estimating local intensity variation in the presence of noise. Overall, the diffusion process converges to PSNR levels comparable to those reported by state-of-the-art methods with less visible blocking/patching artifacts. The method is called locally- and feature-adaptive diffusion **(**LFAD).

The method performs as follows: a) image is over-segmented to *k* approximately equally-sized patches ; b) each patch (region) is diffused individually until a best PSNR is attained; c) adjacent regions are merged based on a similarity metric; d) diffusion repeats for merged regions until PSNR shows improvement or only two regions are left covering the whole image. Subsections below discuss each of the above steps.

6.1 Superpixel segmentation

As discussed above, we need to start with an over-segmented image. For this purpose, we use the superpixel segmentation method with a parameter *k* which is a desired number of approximately equally-sized superpixels. The procedure begins with an initialization step in which *k* initial cluster centers C_i are sampled on a regular *S*- pixel grid space. To produce roughly equally sized superpixels, the grid interval, S is set: $S = \sqrt{N/k}$. The centers are moved to seed locations corresponding to the lowest gradient position in a 3x3 neighborhood, and thus avoid centering a superpixel on an edge. This reduces the chance of seeding a superpixel with a noisy pixel. Next, in the assignment step, each pixel *i* is associated with the nearest cluster center whose search region overlaps its location. The distance measure *D*, determines the nearest cluster center for each pixel. Since the expected spatial extent of a superpixel is a region of approximate size *SxS*, the search for similar pixels is carried in a region of size 2*Sx*2*S* around the superpixel center. Once each pixel has been associated with the nearest cluster center, an update step adjusts the cluster centers to be the mean vector of all the pixels belonging to the cluster. The *L*2 norm is used to compute a residual error *E* between center locations of the new and previous clusters. The assignment and update steps can be repeated iteratively until convergence. Experimentally, twenty iterations are sufficient for most images, therefore, in the rest of the paper we use this value.

6.2 Region (patch) merging

If image *I* is partitioned into sub-regions $R_1, R_2, \ldots, R_{n.}$, the following properties must hold true:

1. $R_1 \cup R_2 \cup \ldots \cup R_n = I$;
2. R_i *is connected;*
3. $R_i \cap R_j$ *is empty.*

The regions are merged based on the similarity metric which is chosen to be the intensity variance. Let us denote a pair of adjacent regions $R_i \sim R_j$ and merged regions $R_i \cup R_j$. The region merging algorithm performs according to the following steps:

1. For $\forall\ R_i \sim R_j$, if $\sigma_j^2 \leq \alpha * \sigma_i^2$ then $R_m = R_i \cup R_j$
2. If $R_m \neq I$, Increment α. Goto Step 1; otherwise
3. Stop.

6.3 Modified diffusion

The normalized inverse difference moment (IDM) characterizes both coarse and fine structures. The IDM has small contributions from homogenous region and larger values from non-homogenous regions. Ranging between 0 and 1, a value of IDM equal to 0 indicates a pixel being part of a homogenous neighborhood. A value equal to 1 indicates that the pixel is a part of texture or an object boundary. The visualized IDM feature is contrasted with the gradient image in Fig. 6.2 IDM is calculated in 9x9 windows centered at pixel (i,j). Fig. 6.3 shows the line profile plots for both IDM and gradient values across the hat area of the "Lena" image with AWG noise σ=40. The figures show that IDM is a robust indicator of the object boundary and texture edges.

The diffusivity function of Eq. 2 is modified to the following:

$$c_p = \exp\left(-\left(\frac{IDM(I)}{\lambda}\right)^2\right), p = N, S, W, E \quad (5),$$

where

$$IDM = 1 - \sum_{i=0}^{G-1} \sum_{j=0}^{G-1} \frac{1}{1 + (i - j)^2} P(i, j) \qquad (6).$$

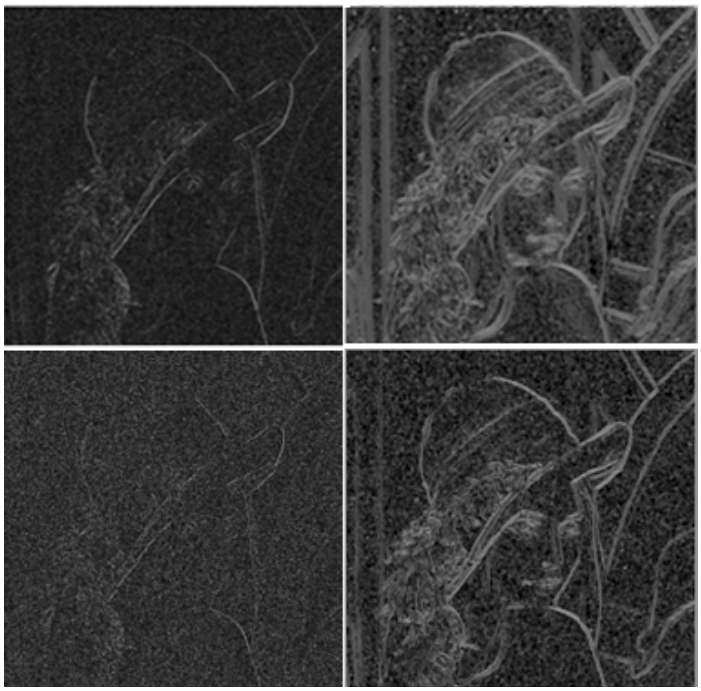

Fig. 6.2 First column: Gradient image for AWG noise σ =20, 40 for "Lena";
Second column: IDM image for AWG noise σ=20, 40.

Given an MxN neighborhood containing G gray levels, let f(m,n) be the intensity at sample m, line n of the neighborhood.

Then

$$P(i, j \mid \Delta x, \Delta y) = W \cdot Q(i, j \mid \Delta x, \Delta y),$$

where

$$W = \frac{1}{(M-\Delta x)(N-\Delta y)};$$

$$Q(i,j \mid \Delta x, \Delta y) = \sum_{n=1}^{N-\Delta y} \sum_{m=1}^{M-\Delta x} A$$

and

$$A = \begin{cases} 1, iff\ (m,n) = i \quad and \quad f(m+\Delta x, n+\Delta y) = j \\ 0, elsewhere \end{cases}$$

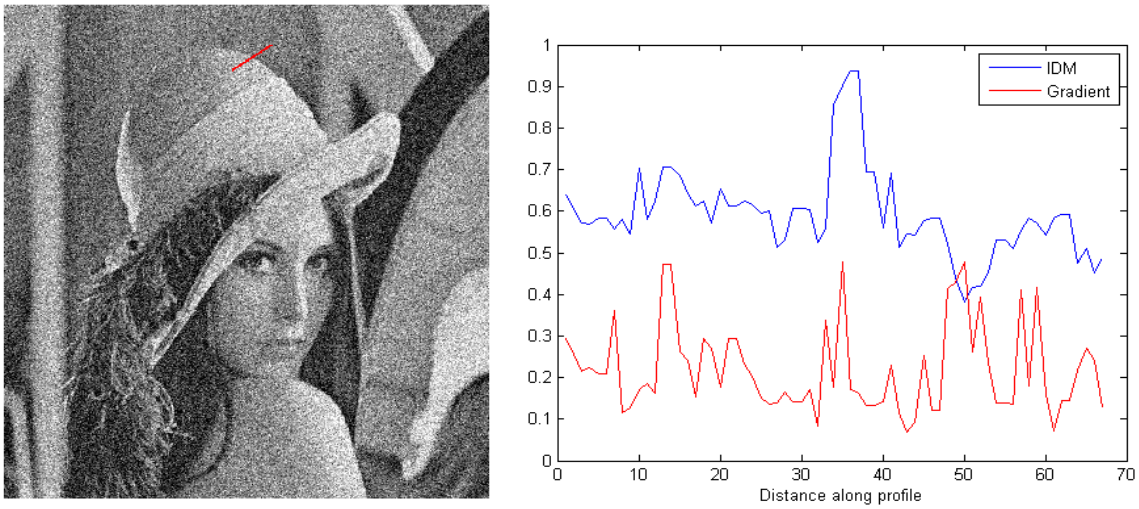

Fig. 6.3 Left: "Lena" image with AWG noise σ =40; Right: IDM and gradient values along a line (red) segment in the "Lena" image.

6.4 Parameter selection: *patch size and diffusion constant*

Levin and Nadler [100] derive bounds on how well any denoising algorithm can perform. The bounds are dependent on the patch size, where larger patches lead to better results. For large patches and low noise, tight bounds cannot be estimated. The result suggests a novel adaptive variable-sized patch scheme for denoising. Chatterjee [101] found that smaller patches can lead to performance degradation from the lack of information

captured by each patch, and large patches might capture regions of widely varying information in a single patch and also result in fewer similar patches being present in the image. It was shown also that clusters with more patches are denoised better than clusters with fewer patches, and the bound on the predicted MSE increases at different rates as the patch size grows from 5x5 to 19x19. Thus, it was concluded that a patch size of 11x11 can capture the underlying patch geometry while offering sufficient robustness in the search for similar patches. The BM3D uses blocks of 8x8 for low noise levels, i.e., $\sigma \leq 40$ and 11x11 for the Wiener filter at the post processing step, and 12x12 patches for hard thresholding of transform coefficients for noise levels with $\sigma > 40$.

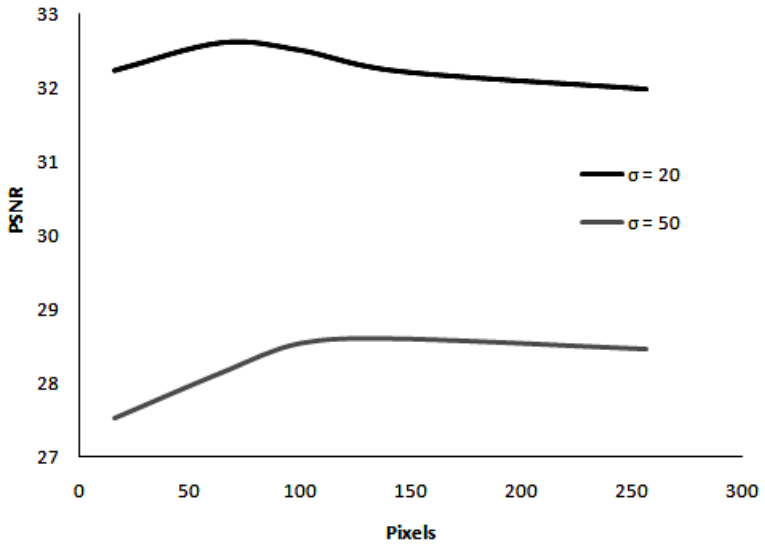

Fig. 6.4 PSNR versus patch size (area in pixels) with AWG noise $\sigma=20$ and $\sigma=50$ for the "Lena" image.

Fig.6.4 displays the relationship between PSNR versus patch area size for noise levels $\sigma=20$ and $\sigma=50$ for the "Lena" image. It clearly shows that for the low noise level

σ=20, PSNR reaches its maximum around a patch area size of 50-80, and for the high noise level σ=50, PSNR reaches its maximum around a patch area size of 110-140. In our work, we calculate the bounds with a patch area of 64 pixels for low noise levels, i.e., σ≤40, and a larger patch of 120 pixels for high noise levels, i.e., σ>40. To make an automatic selection of the patch size, one can use one of several available methods for estimation of the noise standard deviation. For example, one can suppress the image structure using the Laplacian mask such that the remaining part of the image is noise [102].

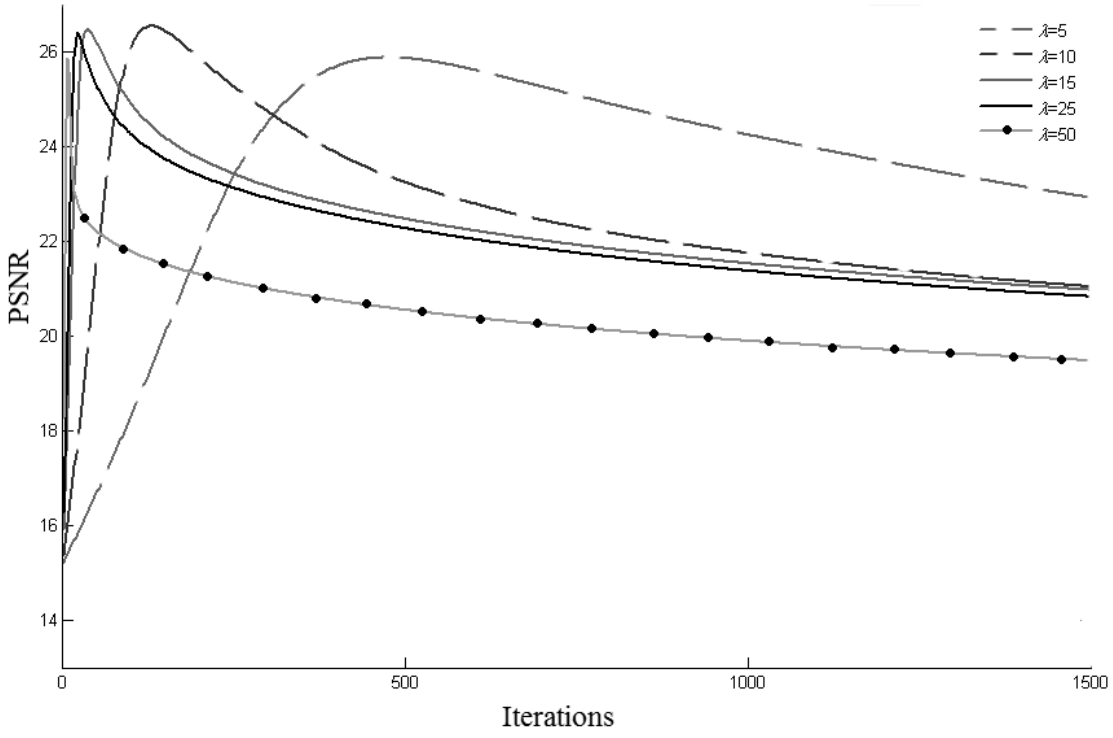

Fig. 6.5 PSNR obtained using IDM with λ=5, 10, 15, 25, and 50 with AWG noise σ=50 for the "Lena" image.

The diffusion equation needs the value of the diffusion constant, λ. Fig. 6.5 displays PSNR values of the outcomes of IDM based diffusion for a fixed noise level (σ=50) with different values of λ (i.e., λ = 5, 10, 15, 25, and 50) for 1000 iterations for the "Lena" image. The plot indicates that λ=10 is the best choice.

6.5 LFAD Algorithm

Let us denote *I* - input image, *k* – number of regions, *m* – number of merging steps, *Var* –intensity variance and *n* is the number of diffusion steps. The method performs according to the following steps:

1. *Initialize m=0, α = 1.1, λ =10. Segment image into k (k≠1) regions.*
2. *Initialize n=0. Calculate PSNR for each region of initial partition, i.e.,* $[PSNR_k^{(0)}]_0$.
3. *Iteration step: Diffuse image pixel* $I_{i,j}$ *using Eq.(4).*
4. *For* $\forall R_i$ *: if* $[PSNR_k^{(n+1)}]_m > [PSNR_k^{(n)}]_m$, *Goto Step 3; else Goto Step 6.*
5. *While* $R_m \neq I$, *for* $\forall$ *Ri ~ Rj, if* $Var(R_j) \leq \alpha^* Var(R_i)$, *then* $R_i \cup R_j$; *m=m+1; update k;, Goto Step 2, else Repeat Step 5 with* $\alpha = \alpha+0.1$.
6. *Stop.*

6.6 Experimental Results

The LFAD is tested on a number of benchmark images degraded by AWG noise of μ=0 and σ = 10, 20, 30, 50, and 100. The comparison is made to other diffusion models such as PM[13], Catte[42], Li [45], LVCFAB[47], GSZFAB[103], and RAAD[104]. We also

compare the method to the state-of-the-art denoising BM3D method. The evaluation is performed first based on PSNR and universal image quality index (UIQI)

Table 6.1. PSNR of the proposed method.

Image/Noise, σ	**LFAD**				
	10	**20**	**30**	**50**	**100**
Lena	35.56	32.61	30.85	28.59	25.56
House	35.94	32.93	31.11	28.68	25.12
Peppers	34.48	31.05	29.03	26.56	23.18
Cameraman	33.99	30.18	28.24	25.89	23.08

Table 6.2 PSNR comparison of different anisotropic diffusion methods for “Lena” image.

Method/ σ	**10**	**20**
Noisy	28.15	22.14
PM	32.70	29.37
Catte	33.27	30.09
Li	34.28	31.15
GSZ FAB	32.49	28.29
LVCFAB	31.90	26.67
RAAD	34.33	31.24
LBPD	34.27	31.17
SWCD	32.45	29.85
LFAD	**35.56**	**32.61**

The above specified parameters were used to obtain Table 6.1, which shows PSNR values by the LFAD for benchmark images. Next, in Table 6.2, the LFAD is compared to

the six diffusion based methods. The improvement by LFAD for the given noise levels ranges from 1.3 dB for low noise to 1.59dB for AWG noise σ=100. It is interesting to note that, compared to the reference PM method, the use of the IDM feature helped with improving PSNR by 0.65db for low noise levels to 1.03 dB for higher noise.

Table 6.3. UIQI comparison of BM3D and LAFD methods.

Noise, σ	**10**		**20**		**30**		**50**		**100**	
Method	**BM3D**	**LFAD**	**BM3D**	**LFAD**	**BM3D**	**LFAD**	**BM3D**	**LFAD**	**BM3D**	**LFAD**
Lena	0.70	0.69	0.61	0.60	0.55	0.54	0.47	0.46	0.34	0.34
House	0.59	0.56	0.45	0.43	0.40	0.38	0.34	0.32	0.27	0.24
Peppers	0.82	0.81	0.74	0.74	0.69	0.68	0.60	0.59	0.47	0.47
Cameraman	0.60	0.59	0.49	0.49	0.43	0.43	0.36	0.35	0.26	0.24

The comparison to the state-of-the-art denoising method, i.e., BM3D, shows that the performance of LFAD is 0.35 dB lower compared to that of the BM3D for noise level σ=10 and 0.39 dB lower for noise level σ=100. Results for BM3D are publicly available at [15] and therefore are not reproduced here. Table 6.3 provides UIQI values by the LFAD and BM3D, and Table 6.4 provides UIQI values by the LFAD and state-of-the-art diffusion models for same benchmark images. It follows from Tables 6.3 and 6.4 that according to this metric the proposed method outperforms the state-of-the-art diffusion models. Only for the "Cameraman" image with AWG noise, σ=10 it shows lower performance. The proposed method shows similar as to BM3D. For high noise, i.e. σ=10 in "Peppers" image, the proposed method outperforms BM3D.

Table 6.4. UIQI comparison of anisotropic diffusion methods.

Method	Image	10	20
GSZ FAB	Lena	0.63	0.48
	Peppers	0.59	0.47
	Cameraman	0.54	0.38
LVCFAB	Lena	0.63	0.43
	Peppers	0.59	0.42
	Cameraman	0.54	0.34
RAAD	Lena	0.68	0.57
	Peppers	0.63	0.54
	Cameraman	**0.60**	0.46
LBPD	Lena	0.68	0.57
	Peppers	0.66	0.57
	Cameraman	0.64	0.52
SWCD	Lena	0.65	0.53
	Peppers	0.64	0.55
	Cameraman	0.53	0.42
LFAD	Lena	**0.69**	**0.60**
	Peppers	**0.81**	**0.74**
	Cameraman	0.59	**0.49**

Fig. 6.6 shows that fewer blocking/ringing artifacts are introduced by LFAD than by the BM3D. The denoising performance of the LFAD is further illustrated in Fig. 6.7 and Fig. 6.8, where we show fragments of noisy (i.e., σ=10, 20, 30, and 50) test images

and corresponding denoised fragments. It is notable that in the regions of smooth intensity transition, the quality of denoising is higher, and lesser or no ringing is observed around contours of extended objects.

Fig. 6.6 First row: "Lena" image and that with AWG noise, σ =100; Second row: Results by BM3D and LFAD. Arrows show areas where LFAD performs comparatively better than BM3D.

Fig. 6.7 First column: “Lena” image with AWG noise, σ =10, 20, 30, and 50; Second column: corresponding results by the LFAD.

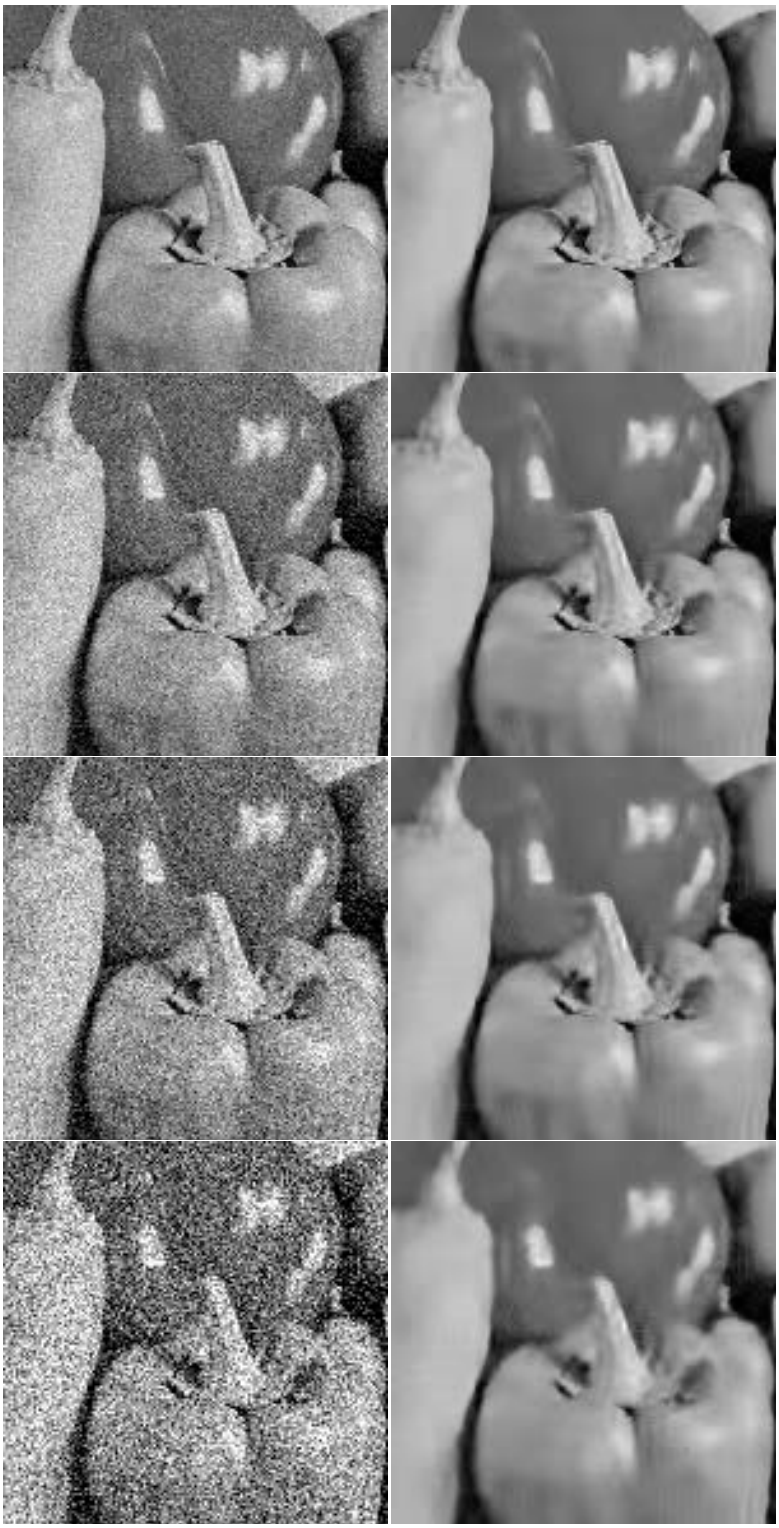

Fig. 6.8 First column: “Peppers” image with AWG noise, σ =10, 20, 30, and 50; Second column: corresponding results by LFAD.

6.7. Conclusion

In this chapter we have proposed a new locally- and feature-adaptive diffusion based method of image denoising from AWG noise. The high performance of the method results from the following properties: a) patch-based optimization of PSNR; b) region merging and repetitive iteration of the process; and c) modification of the diffusion function, i.e. usage of the IDM feature instead of the gradient value. The method has attained the highest performance in the class of advanced diffusion based methods. It is also competitive with the state-of-the-art BM3D method. Visible blocking and ringing artifacts generally inherent to block- and transform-based methods are reduced.

CHAPTER 7

CONCLUSION AND FUTURE WORK

This dissertation has been an investigation of the diffusion process of nonlinear filters as it concerns their capabilities for noise removal, edge preservation and less artifacts in the images. The dissertation introduced methods to improve image quality and explored the theoretical limits of the models' abilities to achieve these improvements. In this final chapter, the results from the previous chapters are summarized and additional research is proposed that can extend the efforts described in the earlier chapters of this dissertation.

This chapter is organized as follows: In section 7.1 a summary of the significant contributions of Chapter III, IV, V and VI is provided. Then, in Section 7.2, areas that are believed to lead to fruitful research that will extend the work performed in this dissertation are discussed.

7.1 Summary of results and contributions

This section provides an overview of major contributions of the dissertation.

7.1.1 Review of results in chapter III. In this chapter, we presented a new image denoising method based on robust M-estimators, which incorporates a robust M-estimators weight functions as a diffusivity function. Based on the evaluation results, the new method shows a higher on PSNR and perceptual quality compared to those of PM method. The major contribution of this chapter is implementation of new diffusivity functions using robust M-estimator weight functions in the diffuson equation.

7.1.2 Review of results in chapter IV. In this chapter, we have described a novel feature-preserving adaptive non-linear diffusion algorithm based on local binary pattern texton.

The proposed method is based on local structure and involves local binary texton for the denoising process. First, we classify the central pixel as edge, spot, flat region, line end or corner using LBP texton. According to different types of pixel texton, relative adjustments to weights of the diffusion are made such that strong diffusion on spot/flat pixels is encouraged whereas edge/line/corner pixels are diffused slower/lesser. We believe this method represents an important step forward for the use of neighborhood design that captures local context in images. Experimental results demonstrate the feasibility of the context based controlled diffusion approach.

7.1.3 Review of results in chapter V. In this chapter, we have presented an adaptive non-linear wavelet diffusion method. Detail coefficients are diffused selectively depends on the energy distribution across the scales in two-level SWT. Shift invariance of SWT allows for accurately gathering the context information in details subbands and thus has contributed to the performance of the method. Unlike other context-based denoising models, here neither segmentation nor edge detection is performed. The method has been compared to a fairly large number of recently developed denoising techniques which explore the adaptation concept for wavelet shrinkage or diffusion. Based on the evaluation results, it can be concluded that the textures and edges are preserved by SWCD and no visual artifacts are created. The proposed method outperforms methods under comparison and that is specifically noticeable for medium noise levels. The implementation is computationally efficient as it does not demand on classification or edge detection.

7.1.4 Review of results in chapter VI. In this chapter, we have proposed a new locally- and feature-adaptive diffusion based method of image denoising from AWG noise. The high performance of the method results stem from the following properties: a) patch-based optimization of PSNR; b) region merging and repetitive iteration of the process; and c) modification of the diffusion function, i.e. usage of the IDM feature instead of the gradient value. The method has attained the highest performance in the class of advanced diffusion based methods. It is also competitive with the state-of-the-art BM3D method. Visible blocking and ringing artifacts generally inherent to block- and transform-based methods are reduced.

7.2 Recommended future research

This section outlines additional research efforts that could be taken to extend the work described in this dissertation. Further research is described that could be performed in the areas of image denoising.

- Robust edge and feature detection to utilize this information in thee diffusivity function.
- Develop a numerical method for diffusion equation which is stable and accurate.
- Develop a method to automatically determine the parameter λ and the size of the window for the implementation.
- Develop a method to automatically determine the stopping criteria for nonlinear diffusion.
- Speeding up the processing by porting operations to the graphics processing unit (GPU).

REFERENCES

1. *Z. Wang and A. C. Bovik***,** A universal image quality index**,** *IEEE Signal Processing Letters*, Vol: 9 No: 3, Page(s): 81-84, March 2002.
2. Z. Wang, A.C. Bovik, H.R. Sheikh, and E.P. Simoncelli. Image quality assessment: From error visibility to structural similarity. IEEE Transactions on Image Processing (TIP), 13(4):600-612, 2004.
3. Z. Wang, E.P. Simoncelli, and A.C. Bovik. Multiscale structural similarity for image quality assessment. In Conference Record of the Thirty-Seventh Asilomar Conference on Signals, Systems and Computers, volume 2, pages 1398{1402. IEEE, 2003.
4. Z. Wang and Q. Li. Information content weighting for perceptual image quality assessment. IEEE Transactions on Image Processing (TIP), 20(5):1185-1198, 2011.
5. H.R. Sheikh, A.C. Bovik, and G. De Veciana. An information fidelity criterion for image quality assessment using natural scene statistics. IEEE Transactions on Image Processing (TIP), 14(12):2117-2128, 2005.
6. H.R. Sheikh and A.C. Bovik. Image information and visual quality. IEEE Transactions on Image Processing (TIP), 15(2):430-444, 2006.
7. A.K. Moorthy and A.C. Bovik. Blind image quality assessment: From natural scene statistics to perceptual quality. IEEE Transactions on Image Processing (TIP), 20(12):3350-3364, 2011.

8. P. Ye and D. Doermann. No-reference image quality assessment using visual codebooks. IEEE Transactions on Image Processing (TIP), 21(7):3129-3138, 2012.
9. Tang, N. Joshi, and A. Kapoor. Learning a blind measure of perceptual image quality. In International Conference on Computer Vision and Pattern Recognition (CVPR). IEEE, 2011.
10. M.A. Saad, A.C. Bovik, and C. Charrier. Blind image quality assessment: A natural scene statistics approach in the dct domain. IEEE Transactions on Image Processing (TIP), 21(8):3339{3352, 2012.
11. Mittal, A. Moorthy, and A. Bovik. No-reference image quality assessment in the spatial domain. IEEE Transactions on Image Processing (TIP), 21(12):4695-4708, 2012.
12. A.K. Moorthy and A.C. Bovik. A two-step framework for constructing blind image quality indices. IEEE Signal Processing Letters, 17(5):513-516, 2010.
13. P. Perona and J. Malik, "Scale-space and edge detection using anisotropic diffusion", *IEEE Transactions on Pattern Analysis and Machine Intelligence*, vol. 12, no. 7, pp. 629–639, 1990.
14. L.I. Rudin, S. Osher, and E. Fatemi. Nonlinear total variation based noise removal algorithms. Physica D, 60:259-268, 1992.
15. C. Tomasi and R. Manduchi, "Bilateral filtering for gray and color images," Proc. Int. Conf. Computer Vision, 1998, pp. 839–846.
16. S. M. Smith and J. M. Brady, "Susan - a new approach to low level image processing," Int. Journal of Computer Vision, vol. 23, pp.45–78, 1997.

17. L. Yaroslavsky, Digital Picture Processing - An Introduction, Springer Verlag, 1985.
18. Kimmel N. Sochen and R. Malladi, “Framework for low level vision,” IEEE Trans. Image Processing, Special Issue on PDE based Image Processing, vol. 7, no. 3, pp. 310–318, 1998.
19. R. Kimmel N. Sochen and A.M. Bruckstein, “Diffusions and confusions in signal and image processing,” Mathematical Imaging and Vision, vol. 14, no. 3, pp. 195–209, 2001.
20. R. Kimmel A. Spira and N. Sochen, “A short time beltrami kernel for smoothing images and manifolds,” IEEE Trans. Image Processing, vol. 16, no. 6, pp. 1628–1636, 2007.
21. M. Elad, “On the origin of the bilateral filter and ways to improve it,” IEEE Trans. Image Processing, vol. 11, no. 10, pp. 1141–1151, October 2002.
22. D Andrews and C Mallows, Scale mixtures of normal distributions, J. Royal Stat. Soc., vol. 36, pp. 99, 1974.
23. J Portilla, V Strela, M Wainwright, E P Simoncelli , Image Denoising using Gaussian Scale Mixtures in the Wavelet Domain, Technical Report TR2002-831, Computer Science Department, Courant Institute of Mathematical Sciences, New York University. September 2002.
24. J Portilla, V Strela, M Wainwright, E P Simoncelli. Image Denoising using Scale Mixtures of Gaussians in the Wavelet Domain. IEEE Transactions on Image Processing. vol 12, no. 11, pp. 1338-1351, November 2003.

25. Buades, B. Coll, and J. Morel, “A non-local algorithm for image denoising,” CVPR , pp. 60–65, June 2005.
26. S. Awate and R. Whitaker, “Higher-order image statistics for unsupervised, information-theoretic, adaptive, image filtering,” CVPR , pp. 44–51, June 2005.
27. M. Aharon, M. Elad, and A. Bruckstein. K-svd: An algorithm for designing overcomplete dictionaries for sparse representation. IEEE Transactions on Signal Processing (TIP), 54(11):4311-4322, 2006.
28. Chatterjee and P. Milanfar, “Clustering-based denoising with locally learned dictionaries,” IEEE Trans. Image Process. , vol. 18, no. 7, pp. 1438–1451, 2009.
29. H. Takeda, S. Farsiu, and P. Milanfar, “Kernel regression for image processing and reconstruction,” IEEE Trans. Image Process. , vol. 16, no. 2, pp. 349–366, 2007.
30. K. Dabov, A. Foi, V. Katkovnik, and K. Egiazarian, “Image denoising by sparse 3D transform-domain collaborative filtering”, *IEEE Transactions on Image Processing*, vol.16, 8, 2007, pp. 2080-2095.
31. D. Zoran and Y. Weiss. From learning models of natural image patches to whole image restoration. In International Conference on Computer Vision (ICCV). IEEE, 2011.
32. T. Ojala, M. Pietikainen, and T. Maenpaa. “Multiresolution gray-scale and rotation invariant texture classification with local binary patterns”. *IEEE Transactions on Pattern Analysis and Machine Intelligence*, 24:971–987, 2002.
33. G.R.J. Cooper, “The Antialiased Textural Analysis of Aeromagnetic Data”, *Computers & Geosciences*, vol. 35, 2009, pp.586-591.

34. T. Iijima. Basic theory on normalization of pattern (in case of typical one-dimensional pattern). Bulletin of the Electrotechnical Laboratory, 26:368–388, 1962.
35. P. Charbonnier, L. Blanc-Feraud, G. Aubert, and M. Barlaud. Two deterministic half-quadratic regularization algorithms for computed imaging. In Proc. 1994 IEEE International Conference on Image Processing, volume 2, pages 168–172, Austin, TX, November 1994. IEEE Computer Society Press.
36. P. Mrazek, J.Weickert, G. Steidl, Diffusion inspired shrinkage functions and stability results for wavelet denoising, Int. J. Computer Vision 64 (2005), 171–186.
37. F. Andreu, C. Ballester, V. Caselles, and J. M. Mazon. Minimizing total variation flow. Differential and Integral Equations, 14(3):321–360, March 2001.
38. S. L. Keeling and R. Stollberger. Nonlinear anisotropic diffusion filters for wide range edge sharpening. Inverse Problems, 18:175–190, January 2002.
39. Gilboa, G., Sochen, N.A., and Zeevi, Y.Y. 2002. Forward-and- backward diffusion processes for adaptiveimage enhancement and denoising. IEEE Transactions on Image Processing, 11(7):689– 703.
40. Weickert, J., Anisotropic Diffusion in image processing, ECMI Series, Teubner, Stuttgart, 1998.
41. Welk, M., Weickert, J., and Steidl, G., A four-pixel scheme for singular differential equations. In R. Kimmel, N. Sochen, and J. Weickert, editors, Scale-Space and PDE Methods in Computer Vision, volume 3459 of Lecture Notes in Computer Science, Springer pages 585.597, Berlin, 2005.

42. F. Catté, P.-L. Lions, J.-M. Morel, and T. Coll, “Image selective smoothing and edge detection by nonlinear diffusion”, *SIAM Journal on Numerical Analysis*, vol. 29, no. 1, pp. 182–193, 1992.
43. V. B. S. Prasath and A. Singh, “Well-Posed Inhomogeneous Nonlinear Diffusion Scheme for Digital Image Denoising”, *Journal of Applied Mathematics*, 2010, ID #763847, 14 pages, 2010. doi:10.1155/2010/763847.
44. J.Yu, J. Tan, Y. Wang, “Ultrasound speckle reduction by a SUSAN-controlled anisotropic diffusion method”, *Pattern Recognition*, 2010, pp. 3083-3092.
45. H. C. Li, P. Z. Fan, and M. K. Khan, “Context-Adaptive Anisotropic Diffusion for Image Denoising”, *IET Electronics Letters*, 48, 14, 2012, pp.827-829.
46. Shin-Min Chao, Du-Ming Tsai, “An improved anisotropic diffusion model for detail- and edge-preserving smoothing”, *Pattern Recognition Letters*, vol. 31,13, 2010, pp. 2012-2023.
47. Y. Wang, L. Zhang, P. Li, “Local Variance-Controlled Forward-and-Backward Diffusion for Image Enhancement and Noise Reduction”, *IEEE Transactions on Image Processing*, 2007, pp.1854-1864.
48. Y. Yu and S.T. Acton, “Speckle reducing anisotropic diffusion”, *IEEE Transactions on Image Processing*, vol. 11, 2002, pp. 1260-1270.
49. Z. Fan, Mo Yoo Yang, Mong Koh Liang, and Kim Yongmin, “Nonlinear Diffusion in Laplacian Pyramid Domain for Ultrasonic Speckle Reduction”, *IEEE Transactions on. Medical Imaging*, vol. 26, 2007, pp. 200-211.
50. K. Z. Adb-Elmoniem **,** A. M., Youssef **, and** Y. M. Kadah, “Real-time speckle reduction and coherence enhancement in ultrasound imaging via nonlinear

anisotropic diffusion", *IEEE Transactions on Biomedical Engineering*, vol. 49, 9, 2002, pp. 997-1014.

51. Bao, Y., and Krim, H., Towards bridging scale-space and multiscale frame analyses, in Wavelets in Signal and Image Analysis, A. A. Petrosian and F. G. Meyer, eds., vol. 19, Computational Imaging and Vision, Kluwer, Dordrecht, 2001, ch. 6.
52. Bruni, V., Piccoliand, B., and Vitulano, D., Wavelets and partial differential equations for image denoising. Electronic Letters on Computer Vision and Image Analysis, 6:36–53, 2008.
53. Lixia Chen, Image De-noising Algorithms Based on PDE and Wavelet, ISCID, vol. 1, pp.549-552, 2008 International Symposium on Computational Intelligence and Design, 2008. DOI: 10.1109/ISCID.2008.196
54. Shih, A.C.-C., Liao, H.-Y.M., Lu, C.-S.: A New Iterated Two-Band Diffusion Equation: Theory and Its Applications. IEEE Transactions on Image Processing (2003) DOI: 10.1109/TIP.2003.809017
55. Welk, M., Weickert, J., and Steidl, G., A four-pixel scheme for singular differential equations. In R. Kimmel, N. Sochen, and J. Weickert, editors, Scale-Space and PDE Methods in Computer Vision, volume 3459 of Lecture Notes in Computer Science, Springer pages 585.597, Berlin, 2005. DOI: 10.1007/11408031_52
56. Yue, Y., Croitoru, M.M., Bidani, A., Zwischenberger, J.B., Jr., J.W.C., Nonlinear Multiscale Wavelet Diffusion for Speckle Suppression and Edge Enhancement in

Ultrasound Images. IEEE Transactions on Medical Imaging 25, 297–311 (2006) DOI: 10.1109/TMI.2005.862737

57. Nikpour, M., Hassanpour, H., Using diffusion equations for improving performance of wavelet- based image denoising techniques, IET-IPR(4), No. 6, December 2010, pp. 452-462
58. Mallat, S., Zhong, S., Characterization of Signals from Multiscale Edges. IEEE Transactions on Pattern Analysis and Machine Intelligence 14, pp. 710–732 (1992) DOI:10.1109/34.142909
59. Glenn R. E., Demetrio Labate, Flavia Colonna: Shearlet-Based Total Variation Diffusion for Denoising, IEEE Transactions on Image Processing 18(2): 260-268, 2009.
60. Weickert, J., Anisotropic Diffusion in image processing, ECMI Series, Teubner, Stuttgart, 1998.
61. Weickert, J., Steidl, G., Mrazek, P., Welk, M., and Brox, T., Diffusion filters and wavelets: What can they learn from each other? In N. Paragios, Y. Chen, and O. Faugeras, editors, *The Handbook of Mathematical Models in Computer Vision*. Springer, New York, 2005.
62. Tukey, J.W., Exploratory Data Analysis. Addison-Wesley Publishers, Cy, 1977.
63. Huber, P.J., Robust Statistics. John Wiley & Sons, NY, 1981.
64. Kashyap, R. L. and Eom, K. N., Robust image modeling techniques with their applications. *IEEE Transactions on Acoustic, Speech and Signal Processing*, 36(8):1313—1325, 1988.

65. Jolion, J. M., Meer, P., and Bataouche, S., ``Robust clustering with applications in computer vision". *IEEE Transactions on Pattern Analysis and Machine Intelligence*, 13:791—802, 1991.

66. Meer, P., Mintz, D., Rosenfeld, A., and Kim, D., ``Robust regression methods for computer vision: A review". *International Journal of Computer Vision*, 6:59—70, 1991.

67. Dave, R.N. and Krishnapuram, R. M-estimators and robust fuzzy clustering, In Fuzzy Information Processing Society, 1996, NAFIPS. 1996, Biennial Conference of the North American, Jun 1996, pp.400-404.

68. Robust window operator. In *Proceedings of Second International Conference on Computer Vision*, pages 591--600, Florida,1988.

69. A. Stein and M. Werman, Robust window operator. In *Proceedings of Second International Conference on Computer Vision*, pages 591--600, Florida,1988.

70. K. V. Arya, P. Gupta, Prem Kumar Kalra, P. Mitra: Image registration using robust M-estimators. Pattern Recognition Letters 28(15): 1957-1968 (2007)

71. Haralick, R. M., Joo, H., Lee, C., Zhuang, X., Vaidya, V., and Kim, M. (1989). Pose estimation from corresponding point data. *IEEE Transactions on Systems, Man and Cybernetics*, 19:1426--1446.

72. Siegel, A. F. , Robust regression using repeated medians. *Biometrika*, 69(1):242—244, 1982.

73. Rousseeuw, P. J., Least median of squares regression'. *Journal of the American Statistical Association*, 79(388):871—880, 1984.

74. N. O. Vil'chevskiy and G. L. Shevlyakov, Robust minimax estimation of a location parameter with a bounded variance. In: V. M. Zolotarev et al. (Eds.), Stability Problems for Stochastic Models (pp. 279{288). TVP/VSP, Moscow/Utrecht, 1994.
75. W.J.J. Rey, Introduction to Robust and Quasi-Robust Statistical Methods, Springer, Berlin, 1983.
76. Muhammad J. Mirza, Kim L. Boyer, *Performance evaluation of a class of M-estimators for surface parameter estimation in noisy range data*, IEEE Transactions on Robotics and Automation 1, 1993, 75-85
77. T. Ojala, M. Pietikainen, and T. Maenpaa. "Multiresolution gray-scale and rotation invariant texture classification with local binary patterns". *IEEE Transactions on Pattern Analysis and Machine Intelligence*, 24:971–987, 2002.
78. Guoying Zhao, MattiPietikäinen: Local Binary Pattern Descriptors for Dynamic Texture Recognition. ICPR (2) 2006.
79. ZhenhuaGuo, Lei Zhang, David Zhang. A Completed Modeling of Local Binary Pattern Operator for Texture Classification. IEEE Transactions on Image Processing, 2010: 1657~1663
80. Rafi Md. Najmus Sadat, Shyh Wei Teng, Guojun Lu, SheikhFaridulHasan: Texture classification using multimodal Invariant Local Binary Pattern. WACV 2011: 315-320
81. Z. Guo, L. Zhang and D. Zhang, "Rotation Invariant Texture Classification using LBP Variance (LBPV) with Global Matching", Pattern Recognition, vol. 43, no. 3, pp. 706-719, Mar. 2010.

82. Xiaoyu Wang, Tony X. Han and Shuicheng Yan, “An HOG-LBP Human Detector with Partial Occlusion Handling,” IEEE International Conference on Computer Vision (ICCV 2009), Kyoto, 2009.
83. Changren Zhu, Hui Zhou, Runsheng Wang, Jun Guo. A Novel Hierarchical Method of Ship Detection from Spaceborne Optical Image Based on Shape and Texture Features. IEEE T. Geoscience and Remote Sensing, 2010: 3446~3456
84. Hao Sun, Cheng Wang, Boliang Wang, Naser El-Sheimy. Pyramid binary pattern features for real-time pedestrian detection from infrared videos. Neurocomputing, 2011: 797~804
85. Di Huang, Caifeng Shan, Mohsen Ardabilian, Yunhong Wang, and Liming Chen, "Local Binary Patterns and Its Applications on Facial Image Analysis: A Survey", IEEE Transactions on Systems, Man, and Cybernetics - Part C: Applications and Reviews, Vol. 41, No. 6, pp. 765 - 781, November 2011.
86. X.Tan and B.Triggs, Enhanced Local Texture Feature Sets for Face Recognition under Difficult Lighting Conditions, IEEE Transactions on Image Processing, 19(6), 1635-1650,2010
87. TimoAhonen, AbdenourHadid, MattiPietikäinen: Face Recognition with Local Binary Patterns. ECCV (1) 2004.
88. TimoAhonen, AbdenourHadid, MattiPietikäinen: Face Description with Local Binary Patterns: Application to Face Recognition. IEEE Trans. Pattern Anal. Mach. Intell. 28(12): 2037-2041 (2006).

89. Guoying Zhao, MattiPietikäinen: Dynamic Texture Recognition Using Local Binary Patterns with an Application to Facial Expressions. IEEE Trans. Pattern Anal. Mach. Intell. 29(6): 915-928 (2007)

90. ValtteriTakala, TimoAhonen, MattiPietikäinen: Block-Based Methods for Image Retrieval Using Local Binary Patterns. SCIA 2005: 882-891

91. Xin Liu, Xinge You, Yiu-ming Cheung. Texture Image Retrieval Using Non-separable Wavelets and Local Binary Patterns. In Proceedings of CIS (1)'2009. pp.287~291

92. Nason, G.P.; B.W. Silverman, The stationary wavelet transform and some statistical applications, Lecture Notes in Statistics, 103, 1995, pp. 281-299.

93. J. Mairal, F. Bach, J. Ponce, G. Sapiro, and A. Zisserman, "Non-Local Sparse Models for Image Restoration," Proceedings of ICCV, 2009.

94. G. Gilboa, S. Osher, "Nonlocal operators with applications to image processing", *Multiscale Modeling & Simulation*, 2009, 7, pp. 1005-1028.

95. G. Peyre, "Image Processing with Non-Local Spectral Bases", SIAM Journal on *Multiscale Modeling and Simulation, 7, 2,* 2008, pp. 703-730.

96. X. Zhang, M. Burger, X. Bresson, and S. Osher, "Bregmanized Nonlocal Regularization for Deconvolution and Sparse Reconstruction", *SIAM Journal on Imaging Sciences*vol. 3, 3, 2010, pp.253-276.

97. K. Dabov, A. Foi, V. Katkovnik, and K. Egiazarian, "A nonlocal and shape-adaptive transform-domain collaborative filtering", In Proc. Int. Workshop on Local and Non-Local Approx. in Image Process., LNLA 2008.

98. C.-A. Deledalle, V. Duval and J. Salmon, "*Non-Local Methods with Shape-Adaptive Patches (NLM-SAP)*", *Journal of Mathematical Imaging and Vision*, 2011, pp. 1-18.

99. R. Achanta, A. Shaji, K. Smith, A. Lucchi, P. Fua, S. Süsstrunk, "SLIC Superpixels Compared to State-of-the-Art Superpixel Methods", IEEE Transactions on Pattern Analysis and Machine Intelligence, vol. 34, 11, 2012, pp.2274-2282.

100. G.R.J. Cooper, "The Antialiased Textural Analysis of Aeromagnetic Data", *Computers & Geosciences*, vol. 35, 2009, pp.586-591.

101. B. Levin and B. Nadler, "Natural Image Denoising: Optimality and Inherent Bounds", In IEEE Conference on Computer Vision and Pattern Recognition (CVPR 2011), 2011.

102. P. Chatterjee and P. Milanfar, "Is Denoising Dead?", *IEEE Transactions on Image Processing*, 19, 4, 2010, pp. 895-911.

103. J. Immerkaer, "Fast Noise Variance Estimation, Computer Vision and Image Understanding", vol. 4, 2, 1996, pp. 300-302.

104. Image and video denoising by sparse 3D transform-domain collaborative filtering Block-matching and 3D filtering (BM3D) algorithm and its extensions http://www.cs.tut.fi/~foi/GCF-BM3D/index.html#ref_results, Last visited on 8/26/2013

VITA

Graduate College
University of Nevada, Las Vegas

Ajay Kumar Mandava

Degrees:
Bachelor of Technology, 2006
Jawaharlal Nehru Technological University, India

Master of Science, 2009
University of Nevada, Las Vegas, USA

Special Honors and Awards:
UNLV, College Best Dissertation Award, 1st place, 2013
UNLV Teaching Assistant Award, UNLV ECE, 2010-2011.
UNLV Summer Scholarship, 2010, 2011.
UNLV Graduate and Professional Student Association (GPSA) grant (2012).
Member of the Honor Society, Phi Kappa Phi.
Member of the Engineering Honor Society, Tau Beta Pi.
Member of the International Honor Society, Golden Key.

Publications:

Book Chapter

1. Jazmin E. Aravena, Markus Berli, ManojMenon, Teamrat A. Ghezzehei, **Ajay K. Mandava**, Emma E. Regentova, Natarajan S. Pillai, John Steude, Michael H. Young, Peter S. Nico and Scott W. Tyler, *"Synchrotron X-ray Microtomography (XMT) – New Means to Quantify Root Induced Changes of Rhizosphere Physical Properties"* , Tomography and Imaging of Soil-Water-Root Processes 2nd edition.

Journal Articles

2. **Ajay K. Mandava**, Emma. E. Regentova, George Bebis *"Locally and Feature-Adaptive Diffusion Based Image Denoising"*, Applied Mathematics & Information Sciences (AMIS), An International Journal, 8(1), 2014, pp. 1-12.
3. **A. K. Mandava**, E. E. Regentova, Speckle Noise Reduction Using Local Binary Pattern, Procedia Technology, 6, 2012, pp.574 - 581.
4. **A. K. Mandava**, E. E. Regentova, Image Diffusion In Connection With Robust M-Estimators, Procedia Engineering, 30, 2012, pp.1138 - 1145.
5. **Ajay K. Mandava**, Emma. E. Regentova, *"Adaptive Image Denoising Based on Non-linear Diffusion in Wavelet Domain"*, Journal of Electronic Imaging 20, 033016 (Sep 14, 2011).

6. Emma E. Regentova, Lei Zhang, **Ajay K. Mandava**, Vijay K. Mandava, Kranthi K. Potetti, Gongyin Chen, Zane Wilson, *"Advantages and Challenges of Radioscopic Detection of Nuclear Materials in Cargo Containers with Two Megavoltage Energy Barriers"*, Journal of Nuclear technology, Vol 175 (1), July 2011, pp.276-285.
7. **Ajay Kumar Mandava**, Emma E. Regentova, Henry Selvaraj, "*Real-time On-Board Object Tracking for Cooperative Flight Control*", Journal of Systems Science, vol.36, no. 2, 2010, pp.15-22.

Conference Articles

1. **Ajay K. Mandava**, Emma. E. Regentova, George Bebis *" FLAD-Feature Based Locally Adaptive Diffusion Based Image Denoising"*, Proceedings of the 2013 International Conference on Image Processing, Computer Vision, & Pattern Recognition, IPCV 2013, July 22-25, 2013, Las Vegas, Nevada, USA, 2 Volumes. CSREA Press 2013.
2. Ali P.Yazdanpanah, E.E. Regentova, **A. K. Mandava**, and G. Bebis, Sky Segmentation by Fusing Clustering with Neural Network, 9th Int. Symp. on Visual Computing, ISVC 2013.
3. **Ajay K. Mandava**, Emma E. Regentova, "*Speckle Noise Reduction Using Local Binary Pattern*", 2nd International Conference on Communication, Computing & Security, 2012.
4. Jazmin E. Aravena, Siul Ruiz, **Ajay Kumar Mandava**, Emma E. Regentova, Teamrat Ghezzehei, Markus Berli, Scott W. Tyler, "*Synchrotron X-Ray Microtomography (XMT) – New Means to Quantify Root Induced Changes of Rhizosphere Physical Properties*", ASA, CSSA and SSSA Annual Meetings 2012, Abstract No: 70451. (2012).
5. **Ajay K. Mandava**, Emma. E. Regentova, K Egiazarian *"Local Binary Pattern Adaptive Diffusion for Image Denoising"*, Proceedings of the 2012 International Conference on Image Processing, Computer Vision, & Pattern Recognition, IPCV 2012, July 16-19, 2012, Las Vegas, Nevada, USA, 2 Volumes. CSREA Press 2012.
6. Jazmin E. Aravena, Siul Ruiz, **Ajay Kumar Mandava**, Emma E. Regentova, Teamrat Ghezzehei, Markus Berli, Scott W. Tyler, *"Simulating root-induced rhizosphere deformation and its effect on water flow"*, AGU 2011, SFO, Dec 5th - Dec 9th, 2011, abstract # H51A-1182.
7. Berli M.; Ruiz S.; Aravena J.E.; Bolduc L.; Ghezzehei T.A.; Cook D.P.; **Mandava A.K.**; Regentova E.E.; Menon M.; Nico P.S.; Tyler S.W.; Young M.H., " *Exploring Rhizosphere Structure Alterations Using X-ray Tomography and Finite Element Calculations."*, DOE Subsurface Biogeochemical Research (SBR) Contractor-Grantee Workshop. US Department of Energy, Office of Science. Washington, DC, 2011.
8. **Ajay K. Mandava**, Emma E. Regentova, *"Image Diffusion In Connection With Robust M-Estimators"*, The International Conference on Communication Technology and system Design, 2012.
9. **Ajay K. Mandava**, Emma. E. Regentova, *"Adaptive Non-linear Diffusion in Wavelet Domain"*, *ICIAR 2011*, Part I, LNCS 6753, pp. 58--68, Springer, Heidelberg (2011).

10. **Ajay K. Mandava**, Latifi Shahram, Emma E. Regentova, *"Reliability Assessment of Microarray Data Using Fuzzy Classification Methods: A Comparative Study"*, ACC 2011, Part I, CCIS 190, pp. 351–360, Springer, Heidelberg (2011).
11. **Ajay Kumar Mandava**, Emma E. Regentova and Markus Berli, *"Image Denoising by Exploring the Context Information in the Wavelet Domain"*, In Advances in Communications, Computers, Systems, Circuits and Devices, European Conference of Circuits Technology and Devices (ECCTD'10), pp.32-36.
12. Pillai, N.S., **A.K. Mandava**, K.K. Potteti, E.E. Regentova and M. Berli, *"Overcoming limits of computer visualization techniques for analyzing physical properties of the rhizosphere"*, *AGU 2010*, SFO, Dec 13th - Dec 17th, 2010, abstract #H13D-1006.
13. E. Regentova, L. Zhang, **A. K. Mandava**, V.K. Mandava et al. , *"Advantages and Challenges of Radioscopic Detection of Nuclear Materials in Cargo Containers with Two Megavoltage Energy Barriers"*, American Nuclear Society, Radiation Protection and Shielding Division, 2010 Topical Meeting, April 18-23, 2010, Las Vegas.
14. **Ajay K. Mandava**, Lei Zhang and E. E. Regentova, *"Radioscopic Inspection of Cargo Containers with Megavoltage Energy Barriers"*, SMC2009, *IEEE conference on Systems, Man and Cybernetics*, 2009, pp.3510 – 3515.
15. L. Zhang, E. E. Regentova, **A. Mandava**, V. Mandava, S. Curtis, *"Radioscopic Cargo Screening for Detecting Nuclear Materials with Megavoltage Dual Energy Barriers"*, HPS 2009 Midyear Proceedings, Recent Advances in Planning and Response to Radiation Emergencies**,** San Antonio, January 31st, 2009, pp.31-39.
16. G. Veni, E. E. Regentova, **A.K. Mandava**, *"A New Method of Detecting Microcalcification Clusters for Computer Aided Digital Mammography"*, Nineteenth International Conference on Systems Engineering (ICSENG 2008), Las Vegas, Aug 19th-21th, 2008, pp532-537.

Dissertation Title:
Nonlinear Adaptive Diffusion Models for Image Denoising

Dissertation Examination Committee:
Chairperson, Emma E. Regentova, Ph.D.
Committee Member, Shahram Latifi, Ph.D.
Committee Member, Venkatesan Muthukumar, Ph.D.
Committee Member, Henry Selvaraj, Ph.D.
Graduate Faculty Representative, Ajoy K. Datta, Ph.D.